Experimental investigation of compaction behaviour of lunar highlands regolith simulant using a second-generation lunar vibratory drum roller

Akshay K. Agarwal,[1] Brendan T. Scott, Ph.D.,[1] and Mark B. Jaksa, Ph.D.[1]

[1]School of Civil Engineering and Construction Management, Adelaide University, SA, 5005, Australia; e-mail: akshaykumar.agarwal@adelaide.edu.au

ABSTRACT

The construction of future lunar infrastructure will require efficient ground improvement techniques capable of increasing the density and load-bearing capacity of lunar regolith to support foundations, landing pads, mobility corridors, and in situ resource utilisation (ISRU) facilities. This study presents the development and experimental evaluation of a second-generation lunar vibrating drum roller (LVDR-2) scale model, incorporating an internally mounted eccentric mass to more closely replicate the operating principle of full-scale vibratory compaction equipment. Laboratory experiments were conducted using engineering-grade lunar highlands regolith simulant (LHS-1E) to investigate the coupled influence of translational speed, vibration frequency, and eccentric mass on compaction performance. Surface settlement and vertical pressures were initially measured to identify the optimum operating combination. The highest peak pressure was recorded at a translational speed of 4 km/h, a vibration frequency of 40 Hz, and an eccentric mass of 75.8 g. This combination was subsequently adopted for detailed geotechnical investigations involving surface settlement, vertical pressure, cone penetration resistance, bulk density, and vane shear strength measurements. The optimised LVDR-2 model demonstrated enhanced compaction performance, characterised by greater surface settlement, higher cone penetration resistance, increased bulk density, and deeper stress transmission within the simulant compared with the earlier LVDR-1 model. These findings provide important design guidance for the development of mechanised lunar ground improvement systems supporting future lunar infrastructure construction.

KEYWORDS: lunar infrastructure development, vibrating smooth drum roller, eccentric mass, vibration frequency, compaction behavior, translational speed.

1. INTRODUCTION

The National Aeronautics and Space Administration (NASA) Artemis programme aims to establish a sustained human presence on the Moon, with future missions focused on long-term exploration, infrastructure development, and scientific operations within the lunar South Pole region [1]. For long-term lunar infrastructure, surface preparation and ground improvement will be essential to improve bearing capacity, reduce settlement, and support repeated mobility and construction operations.

Lunar regolith is an unconsolidated granular material formed through prolonged meteoroid impacts, thermal cycling, and space weathering processes over billions of years [2]. The engineering behaviour of lunar regolith differs substantially from terrestrial soils due to the Moon’s reduced gravitational acceleration, vacuum environment, absence of water, extreme temperature fluctuations, and highly angular particle morphology [3]. These conditions significantly influence particle interaction, stress transmission, and compaction behaviour, thereby limiting the direct transferability of terrestrial construction methodologies to lunar environments.

Transporting large quantities of construction material from Earth is economically and logistically impractical; therefore, future lunar construction will rely heavily on in situ material handling, excavation, levelling, compaction, and stabilisation of lunar regolith [4, 5]. Although returned Apollo samples have provided an important understanding of lunar regolith behaviour, the limited quantity of available lunar material restricts large-scale experimental testing [2].

To address these challenges, several recent studies have investigated the adaptation of terrestrial compaction techniques for lunar surface preparation using lunar highland regolith simulants, which are widely adopted as terrestrial surrogates for experimental investigation [6–9]. LHS-1E (previously known as MAB-1 mixed anorthosite and basalt), an engineering-grade lunar highland regolith simulant composed primarily of anorthosite and basalt, has been employed in several recent investigations because its geotechnical properties are representative of lunar highland regolith [10, 11].

The success of future lunar construction activities will depend strongly on the ability to mechanically improve and stabilise the lunar surface to facilitate the construction of roads, landing pads, foundations, and other critical infrastructure required for sustained lunar exploration [1, 12]. Compaction is one of the most widely used terrestrial methods for improving granular soils, as it increases density through particle rearrangement and void reduction [13, 14]. As outlined in NASA’s Excavation, Construction and Outfitting strategic framework within the Space Technology Mission Directorate, a key performance objective is to achieve an in situ density of 1900 kg/m^3 for compacted regolith [15]. Therefore, the development of lightweight and effective mechanised compaction systems is essential for future lunar surface construction. However, the suitability of different compaction methods for lunar regolith remains insufficiently understood, particularly under dry, cohesionless, low-gravity and vacuum-relevant conditions.

Scott et al. [16] demonstrated that rolling dynamic compaction (RDC) can improve the density of dry LHS-1E, thereby establishing the feasibility of adapting terrestrial ground improvement techniques for lunar applications. Subsequently, Agarwal et al. [6] evaluated six industrial ground improvement techniques for potential lunar application and identified vibrating smooth drum rollers (VSDRs) and RDC as the two most promising compaction techniques for lunar surface preparation.

Building upon these findings, Agarwal et al. [7] conducted a direct comparative investigation of these two compaction techniques and demonstrated that the VSDR compaction technique, produced greater surface settlement, higher subsurface pressures, improved density enhancement, and a larger depth of influence than RDC, indicating superior compaction efficiency for lunar highland regolith simulant. Thereafter, Agarwal et al. [17] systematically investigated the influence of translational speed, vibration frequency, and roller mass on the compaction performance of the lunar vibrating drum roller (LVDR-1) scale model and identified higher vibration frequency as the dominant parameter governing subsurface stress transmission and dynamic response. Further investigation by Agarwal et al. [18] demonstrated that improved compaction performance was generally associated with lower translational speed, higher vibration frequency, and heavier roller mass.

Despite these advances, several important research gaps remain regarding the optimisation of vibratory drum roller design and the mechanistic understanding of lunar regolith compaction. Previous investigations primarily focused on the first-generation scale model (LVDR-1) in which additional mass was externally attached above the roller frame, rather than via an internally rotating eccentric loading mechanism representative of conventional vibratory drum rollers. Consequently, the influence of an eccentric loading configuration on vibratory energy transmission, stress propagation, and densification behaviour within LHS-1E remains insufficiently understood. In addition, limited research has investigated how modifications to roller geometry, including drum aspect ratio, influence compaction performance and subsurface response under vibratory loading conditions on LHS-1E. Previous experimental systems also relied on manually adjusted vibration control methods, limiting the precision of vibratory loading during testing. Furthermore, limited information was available on whether the vibration response measured before surface contact remained consistent once the roller engaged with the simulant during compaction. These limitations are significant because future lunar compaction systems must maximise densification efficiency while minimising transported mass and mechanical complexity for extraterrestrial construction applications.

To address these gaps, the present study investigates the compaction behaviour of LHS-1E using a second-generation scale model of a lunar vibrating drum roller (LVDR-2). The study was conducted in two phases. First, a parametric optimisation phase was performed to identify the most effective operating combination of translational speed, vibration frequency, and eccentric mass. Second, detailed geotechnical testing was undertaken using the most prominent optimal operating combination to evaluate the resulting densification behaviour and mechanical improvement of the simulant through surface settlement measurements, earth pressure monitoring, acceleration response analysis, in situ density testing, mini-cone penetration testing, and vane shear testing.

The novelty of this study lies in the systematic optimisation of speed, vibration frequency, and eccentric mass for the LVDR-2 model, followed by detailed geotechnical validation. This integrated approach provides new insight into the mechanisms of vibratory compaction of LHS-1E and informs the development of future lunar surface preparation systems. The findings demonstrate the potential applicability of vibratory roller-based compaction for lunar surface preparation and contribute to the development of scalable surface improvement methodologies for future lunar infrastructure construction.

2. STAGE 1 METHODOLOGY

Two test bins (Bins A and B), each measuring 750 mm in width, 1060 mm in length, and 1200 mm in depth, were used to contain the lunar highland regolith simulant (LHS-1E), as illustrated in Figure 1. The simulant was placed to a depth of 380 mm within each bin, providing sufficient depth to accommodate stress propagation beneath the roller while minimising boundary effects during vibratory compaction. A steel separator plate was installed between the bins to prevent stress transfer and material interaction between the two test sections during vibratory loading. Two large, instrumented soil bins were positioned beneath the elliptical track, however, they can be translated perpendicular to the roller's direction of travel to allow for better access for bin filling and testing. The vibrating smooth drum roller scale model was mobilised using a chain-driven carriage system powered by a variable-speed electric motor, enabling controlled and repeatable translational motion throughout the experimental test.

Preliminary testing was undertaken to identify the optimal combination of operating parameters, including translational speed, vibration frequency, and eccentric mass. This experimental phase was conducted to evaluate the influence of different parameter combinations on the compaction response of the simulant and to determine the operating parameters producing the most effective compaction performance for the LHS-1E simulant. Further details regarding the scale model test rig, scaling methodology, and operating mechanism are provided by Chung et al. [19].

Figure 1. Scale model test rig showing the test bins filled LHS-1E and the chain-driven carriage system used to mobilise the LVDR-2 model.

The LVDR-1 scale model, utilised in earlier experimental investigations [7, 17, 18] and illustrated in Figure 2a, incorporated a drum roller mass of 2.92 kg. To investigate higher mass combinations in the LVDR-1 model, four rectangular steel blocks were affixed to the frame above the drum roller. Although this approach enabled controlled variation of roller mass during previous investigations, it introduced a limitation in the experimental test, as the additional mass was externally attached rather than incorporated as eccentric mass within the drum. Consequently, the vibratory mechanism did not fully replicate the operational behaviour of conventional vibratory smooth drum rollers, in which vibration is generated through the rotation of an internally mounted eccentric mass [20].

To address this limitation, an improved second-generation scaled model, LVDR-2, was developed for the present study. The LVDR-2 model incorporated a 3D-printed drum mounted to a rigid aluminium chassis as shown in Figure 2b, providing enhanced structural stiffness and improved vibration transmission. In the LVDR-2 model, an internally mounted electric motor fitted with an eccentric mass was incorporated into the roller drum to generate controlled vibratory loading, thereby more closely reproducing the vibration-generation mechanism employed in full-scale vibratory compaction equipment [20, 21]. The vibration frequency was regulated through motor speed control by using a GUI (graphical user interface), thereby enabling consistent and repeatable operating parameters during testing.

In addition of the eccentric loading system, the geometric characteristics of the drum were refined. In the present study, the aspect ratio was defined as the ratio of drum diameter to drum width. The LVDR-1 model employed an aspect ratio of approximately 0.6, whereas the LVDR-2 model adopted an increased aspect ratio of 0.8. The LVDR-2 scale model incorporates a drum width of 250 mm and a drum diameter of 200 mm, representing a geometrically scaled approximation of conventional terrestrial vibratory rollers. Drum geometry, including the relationship between drum diameter and width, plays an important role in governing contact area, stress distribution, and the efficiency of energy transmission during vibratory compaction processes [20, 22].

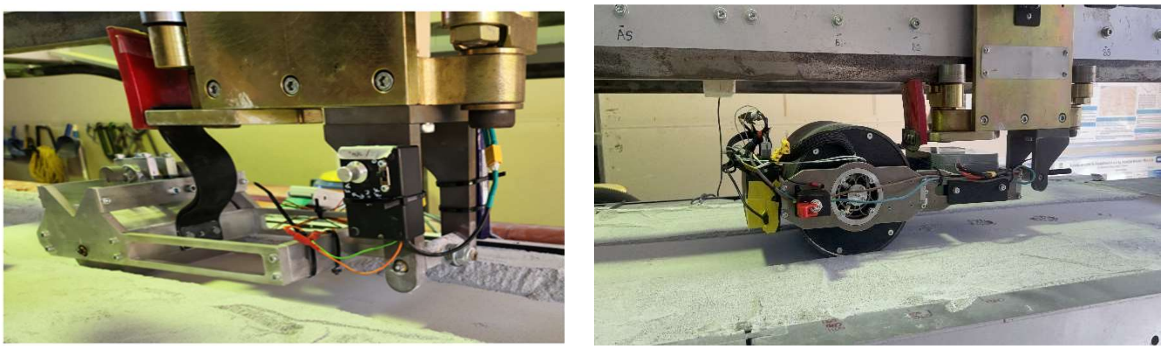

(a) **(b)**

Figure 2. Scale model: (a) LVDR-1 (2.92 kg version) and (b) LVDR-2.

The bespoke earth pressure cells (EPCs) utilised in this study, illustrated in Figure 3a, are 19 mm in diameter and include integrated tri-axial accelerometers, as shown in Figure 3b. Conventional EPCs with larger diameters have been widely employed in geotechnical engineering for in situ earth pressure measurements under terrestrial conditions [23, 24]. However, the reduced dimensions of the bespoke sensors adopted in the present study enabled pressure measurements within the scaled experimental setup while minimising disturbance to the surrounding lunar highland regolith simulant. Each EPC–accelerometer assembly was connected to a custom-built data acquisition system interfaced with a dedicated LabVIEW program, enabling simultaneous real-time measurement of contact pressures and local acceleration response during vibratory compaction. Prior to testing, all EPCs were zeroed to eliminate the influence of overburden pressure, thereby ensuring that only roller-induced dynamic stresses were recorded. At each depth, peak pressure values were determined by averaging measurements obtained from 10 roller passes under each operating combination.

To ensure accurate capture of peak pressure responses and high-frequency vibration effects during compaction, a sampling frequency of 7500 Hz was adopted. The integrated tri-axial accelerometers additionally provided supplementary information regarding the dynamic response and compaction behaviour of the simulant throughout the experimental testing.

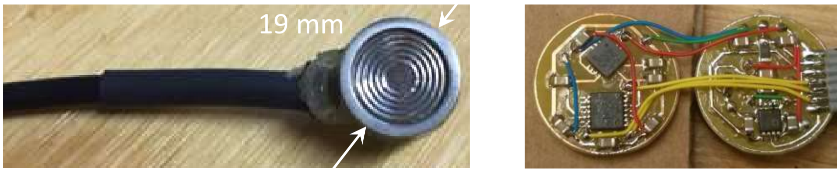

(a) **(b)**

Figure 3. Earth pressure cell: (a) Plan view; (b) Internal 3-axis accelerometers.

Figure 4 illustrates the rolling direction and the position of earth pressure cells (EPCs) within Bins A and B. The two bins were configured as mirror images with respect to EPC placement to ensure consistency and uniformity in data acquisition across the test section. As shown in Figure 4a, the LVDR-2 model traversed a centre lane within each bin to minimise boundary effects during vibratory compaction. For the LVDR-2 model, the rolling direction was maintained from Bin A to Bin B, as shown in Figure 4.

The EPCs were positioned along the bin centreline and maintained at a distance of 375 mm from the bin walls, thereby reducing the influence of the side walls on stress distribution within the simulant. Additional lateral spacing was maintained to allow trial testing to be conducted within both bins throughout this phase of experimental testing. A total of six EPCs were installed, three in each bin with sensors embedded in the LHS-1E with a lateral spacing of 100 mm with respect to each other and at vertical depths of 100, 200 and 300 mm, as illustrated in Figure 4b. At each depth, two EPCs were installed (one in each bin), and the average of the recorded pressure was used to determine the peak pressure at that depth. This setup was adopted to minimise experimental variability and to mitigate the influence of sensor shadowing effects beneath the roller centreline, as reported by Dave and Dasaka [25].

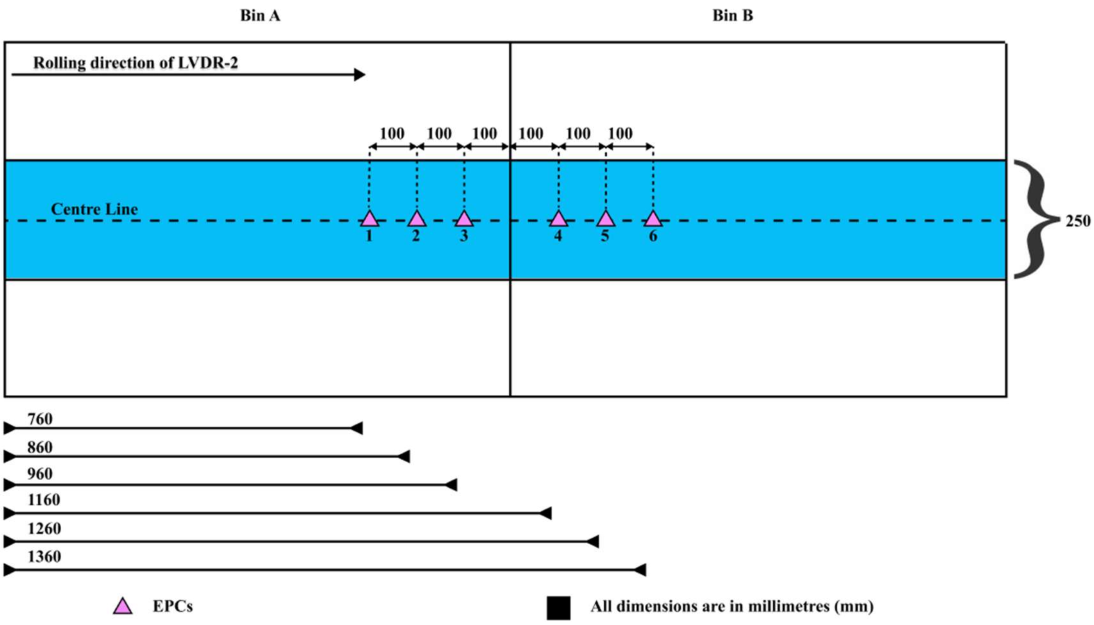

(a)

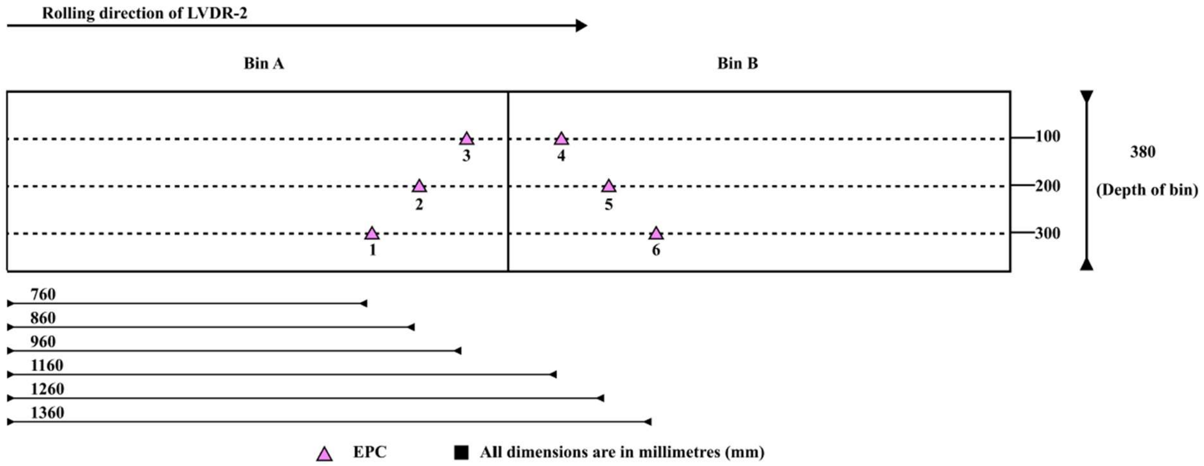

(b)

Figure 4. Arrangement of earth pressure cells (EPCs) within the LVDR-2 test bins: (a) Plan view showing the roller path and EPC locations; (b) Elevation view illustrating the embedment depths and vertical spacing of the EPCs.

To identify the optimal operating combination of translational speed, vibration frequency, and eccentric mass, a series of controlled laboratory experiments was conducted to evaluate their influence on the compaction behaviour of LHS-1E under terrestrial laboratory conditions. Three operating speeds of 1 km/h, 4 km/h, and 7 km/h were adopted, while vibration frequencies of 30 Hz, 35 Hz, and 40 Hz were applied, resulting in nine speed–frequency combinations. These combinations were subsequently evaluated under three eccentric masses, i.e., 21.8 g, 49.8 g, and 75.8 g, yielding a total of 27 distinct test combinations.

A minimum translational speed of 1 km/h was selected based on the findings of Henrich [26], who identified an optimal operating speed range of approximately 1–4 km/h for vibratory rollers. A maximum speed of 7 km/h was selected to extend beyond this range and to facilitate comparison with previous investigations involving the LVDR-1 model, in which a translational speed of approximately 6 km/h at 40 Hz produced the most effective compaction response [17].

For initial compaction passes, LVDR-2 incorporated a drum mass of 4.5 kg and was fitted with an eccentric mass of 21.8 g. Eccentric masses of 49.8 g and 75.8 g were subsequently introduced to evaluate the influence of dynamic loading amplitude on compaction behaviour. The eccentric masses were mounted to the motor shaft within the drum frame without direct contact with the drum shell. Rotation of the eccentric mass generates periodic inertial forces, resulting in dynamic frequency of the roller drum. Variation in eccentric mass directly influences the amplitude of dynamic loading generated by a vibratory drum roller and, consequently, affects compaction efficiency through changes in vibratory energy transfer [20, 27, 28].

Vibration frequencies applied during testing were verified using Fast Fourier Transform (FFT) analyses performed on the signals obtained from the EPCs. The FFT analyses confirmed the operational vibration frequencies associated with each combination, thereby ensuring accuracy and consistency in the applied dynamic loading parameters.

Prior to executing the different test combinations, a preliminary compaction phase was undertaken to induce the majority of initial surface settlement and minimise subsequent densification effects during systematic testing. This preliminary compaction phase comprised 50 passes of the LVDR-2 model at a baseline translational speed of 1 km/h and a vibration frequency of 25 Hz, using the lightest eccentric mass (21.8 g). A preliminary compaction phase was undertaken to induce initial surface settlement before the parametric investigation. The initial roller passes promoted particle rearrangement and progressive densification, consistent with the fundamental mechanisms of vibratory compaction reported in literature [20, 22]. The use of a lower vibration frequency during this stage enabled controlled initial densification while limiting excessive dynamic loading effects on simulant.

Following the preliminary compaction phase conducted at 25 Hz and 1 km/h, the remaining two translational speeds (4 km/h and 7 km/h) were also evaluated at 25 Hz for the lightest eccentric mass configuration of 21.8 g to maintain consistency in the staged testing sequence prior to commencement of the primary testing combinations. Although these additional 25 Hz tests were conducted as part of the staged testing program, they are included in Table 1 using roman numerals, as they were not considered part of the 27 primary test combinations. Following this, the same sequence of translational speeds was systematically repeated at vibration frequencies of 30 Hz, 35 Hz, and 40 Hz. Upon completion of testing for the 21.8 g eccentric mass configuration, the eccentric mass was increased to 49.8 g, and the same sequence of vibration frequencies and translational speeds was repeated. Following completion of this stage, the eccentric mass was further increased to 75.8 g, and an identical testing sequence conducted. The complete experimental program is summarised in Table 1.

This structured methodology enabled systematic evaluation of the coupled effects of translational speed, vibration frequency, and eccentric mass on stress transmission and compaction behaviour for LHS-1E. By maintaining identical initial material conditions throughout the experiment, variability associated with simulant preparation was minimised, consistent with established experimental practice in vibratory compaction studies [22]. Translational speeds of the LVDR-2 model, initially measured in mm/s, were converted to full-scale equivalents in km/h using established scaling relationships [29].

Table 1. Experimental test matrix and operating parameters for LVDR-2 compaction testing.

Combination	Eccentric Mass (g)	Speed (km/h)	Speed (mm/sec)	Vibrating frequency (Hz)	Number of Passes
i		1	21	25	0-50
ii		1	21	25	51-60
iii		4	85	25	61-70
iv		7	150	25	71-80
1		1	21	30	81-90
2		4	85	30	91-100
3	Mass A (21.8 g)	7	150	30	101-110
4		1	21	35	111-120
5		4	85	35	121-130
6		7	150	35	131-140
7		1	21	40	141-150
8		4	85	40	151-160
9		7	150	40	161-170
10		1	21	30	171-180
11		4	85	30	181-190
12		7	150	30	191-200
13		1	21	35	201-210
14	Mass B (49.8 g)	4	85	35	211-220
15		7	150	35	221-230
16		1	21	40	231-240
17		4	85	40	241-250
18		7	150	40	251-260
19		1	21	30	261-270
20		4	85	30	271-280
21		7	150	30	281-290
22		1	21	35	291-300
23	Mass C (75.8 g)	4	85	35	301-310
24		7	150	35	311-320
25		1	21	40	321-330
26		4	85	40	331-340
27		7	150	40	341-350

Surface settlement measurements were conducted along the centreline of the test lane to quantify vertical deformation of the simulant. A standard tape measure was used in conjunction with fixed reference bolts installed on the test rig frame, providing stable and repeatable datum points throughout the experiment. Settlement measurements were recorded at 150 mm intervals along the centreline of the test lane within each bin following completion of each test combination. For each operating combination, the LVDR-2 model completed a total of 10 passes, after which 10 settlement measurements, comprising five measurements within each bin, were obtained and averaged to determine the surface settlement response. Initial measurements obtained prior to compaction (0-passes) were treated as the baseline, thereby enabling the influence of subsequent compaction passes on surface settlement behaviour to be evaluated.

3. STAGE 1 RESULTS AND DISCUSSION

Compaction testing was conducted to evaluate the influence of translational speed, vibration frequency, and eccentric mass on the compaction response of LHS-1E. The primary objective of this testing phase was to identify the optimal operating combination which is capable of producing the most effective densification behaviour prior to undertaking detailed geotechnical investigations. Key response parameters, including surface settlement and peak vertical pressure, were analysed to assess the effectiveness of each operating combination. The findings from Stage 1 testing were used to determine the operating parameters adopted in Stage 2.

Figure 5 presents the average surface settlement as a function of the number of compaction passes performed using the LVDR-2 model along the centre test lane. The results indicate that settlement was greatest during the initial stages of compaction, which is consistent with established soil mechanics principles that loose granular soils experience substantial early densification through particle rearrangement and void reduction under applied compactive effort [13, 30]. This trend is also consistent with previous investigations on LHS-1E by Agarwal et al. [6, 7, 17, 18], which similarly reported that settlement was greatest during the initial stages of compaction, primarily due to the initially loose packing condition of the simulant.

Approximately 8 mm of surface settlement was recorded within the first 20 passes, after which the rate of settlement decreased substantially. As described previously, the initial 50 passes were conducted at a translational speed of 1 km/h, a vibration frequency of 25 Hz, and an eccentric mass of 21.8 g. Beyond this stage, different combinations of translational speed and vibration frequency were applied while maintaining the eccentric mass of 21.8 g to further evaluate the compaction response of the simulant. Between the 50th and 170th pass, testing conducted using the 21.8 g eccentric mass produced only minor additional settlement, despite variations in roller translational speed and vibration frequency. This behaviour indicates that the dynamic loading generated under the lowest eccentric mass configuration produced limited additional densification following the initial settlement phase.

A notable increase in surface settlement was observed after the 180th pass, following an increase in eccentric mass from 21.8 g to 49.8 g. This behaviour indicates that increasing the eccentric mass increased the magnitude of dynamic stresses transmitted into the simulant, resulting in greater surface deformation.

Following completion of the 260th pass, the eccentric mass was further increased from 49.8 g to 75.8 g, and testing was repeated using the same combinations of translational speed and vibration frequency adopted for the previous eccentric mass configurations. During this stage, lower vibration frequencies of 30 and 35 Hz produced negligible additional settlement, indicating that these frequencies generated limited additional densification. However, following an increase in vibration frequency from 35 Hz to 40 Hz after the 320th pass, an additional increase in settlement was observed. Surface settlement reached approximately 24 mm by the 350th pass. Overall, the results indicate that the combination of heavier eccentric mass and higher vibration frequency enhanced the compaction performance of the LVDR-2 model, suggesting a coupled influence of eccentric mass and vibration frequency on the settlement response.

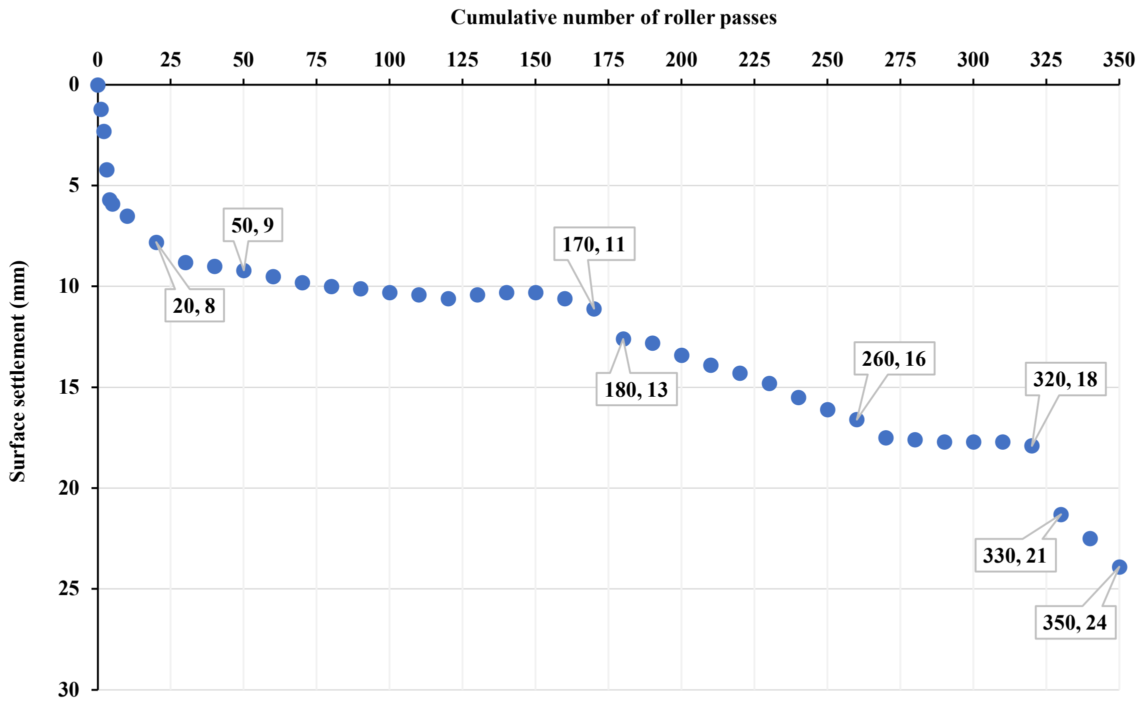

Figure 5. Surface settlement versus cumulative number of passes.

Figure 6 illustrates the dynamic pressure response of LHS-1E during the 230th pass of LVDR-2 operating at a translational speed of 7 km/h, a vibration frequency of 35 Hz, and an eccentric mass of 49.8 g. Pressure measurements obtained from EPCs 1 and 6, 2 and 5, and 3 and 4, installed at depths of 100 mm, 200 mm, and 300 mm, respectively, indicate that peak vertical pressures were greatest near the surface and progressively decreased with increasing depth. This behaviour is consistent with previous vibratory compaction investigations, which similarly reported attenuation of roller-induced dynamic stresses with depth beneath the roller drum [6, 7, 17, 18, 23, 31].

The time at which each EPC recorded the peak pressure varied according to the sensor location within the test bins, consistent with the EPC arrangement illustrated previously in Figure 4. The pressure responses shown in Figure 6 exhibit oscillatory fluctuations throughout the 5-second measurement interval due to the cyclic vibration generated by the rotating eccentric mass within the vibratory drum mechanism. These fluctuations are additionally associated with transient roller–simulant interaction during cyclic drum loading, consistent with observations reported by Mooney and Rinehart [22] and Richart et al. [31].

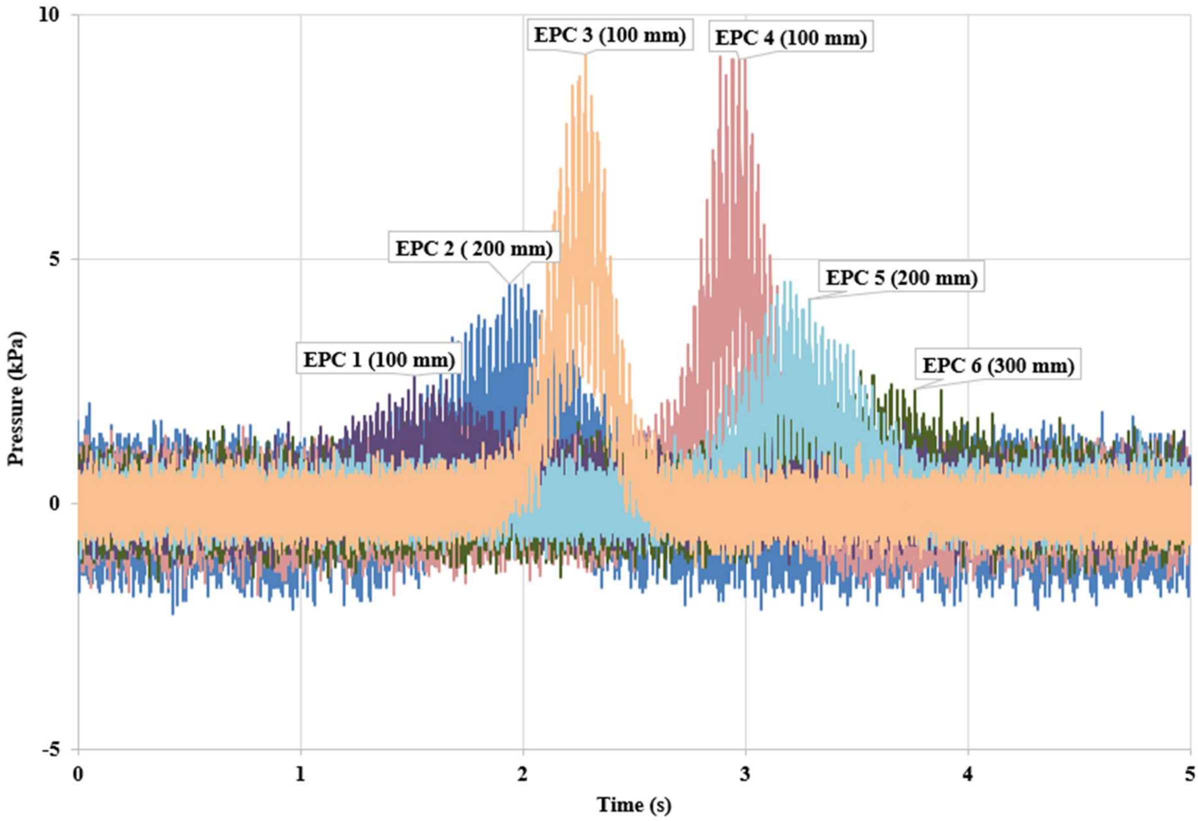

Figure 6. Measured dynamic pressure response obtained from the EPCs during Pass 230; 7 km/h translational speed, 35 Hz vibration frequency, eccentric mass 49.8 g.

Figure 7 presents the measured peak vertical pressures with depth for varying vibration frequencies (30 Hz, 35 Hz, and 40 Hz) under eccentric masses of 21.8 g, 49.8 g, and 75.8 g, (hereafter referred to as Mass A, Mass B, and Mass C, respectively). For each test combination, the peak pressure responses recorded from the six EPCs, installed at depths of 100 mm, 200 mm, and 300 mm (with two EPCs buried at each depth as previously shown in Figure 4b), were averaged. In addition, the reported peak pressures were also averaged over 10 roller passes conducted for each operating combination to minimise experimental variability and improve the repeatability of the measurements.

The results are presented for constant translational speeds of 1 km/h (Figure 7a), 4 km/h (Figure 7b), and 7 km/h (Figure 7c). From Figure 7, it is evident that the combination of Mass C (75.8 g) and a vibration frequency of 40 Hz produced the most effective compaction response across all operating speeds. Under the operating combinations of eccentric Mass C (75.8 g) and 40 Hz frequency, the measured peak pressures at depths of 100 mm, 200 mm, and 300 mm were approximately 20 kPa, 7 kPa, and 4 kPa, respectively, at a translational speed of 1 km/h. At 4 km/h, the corresponding peak pressures increased to approximately 27 kPa, 8 kPa, and 5 kPa, respectively, whereas at 7 km/h the measured peak pressures were approximately 24 kPa, 6 kPa, and 5 kPa.

The findings further suggest that an operating speed of 4 km/h combined with a vibration frequency of 40 Hz and eccentric Mass C (75.8 g) represented the most effective operating parameters among the various combinations investigated in the present study. The enhanced pressure response observed at the intermediate translational speed may be attributed to a more favourable balance between vibration impact spacing, contact duration, and vibratory energy transmission into the simulant.

This finding contrasts with the previous LVDR-1 model, in which lower roller speed i.e., 2 km/h, produced better compaction outcomes [18]. In the present LVDR-2 model, however, the intermediate speed i.e., 4 km/h, showed improved performance, indicating a discrepancy between the two scaled roller configurations. To examine this further, the present results were compared with previous studies on full-scale vibratory rollers. Henrich [26] suggested that vibratory compactors generally operate effectively within a travelling speed range of approximately 1–4 km/h, indicating that effective compaction occurs within a moderate operating speed range. Therefore, the findings provide confidence that the LVDR-2 scale model captures behaviour representative of a full-scale vibratory roller system. Across all the scaled experimental testing performed, speeds in the range of approximately 2–4 km/h appear to provide favourable compaction performance for lunar simulant.

At lower speeds (1 km/h), excessive localised loading and repeated vibration over the same region may have limited efficient stress propagation, whereas at higher speeds (7 km/h), the reduced number of vibration cycles per unit distance likely diminish the transfer of dynamic compaction energy into the underlying layers, consistent with previous vibratory compaction studies [17, 18, 21, 22].

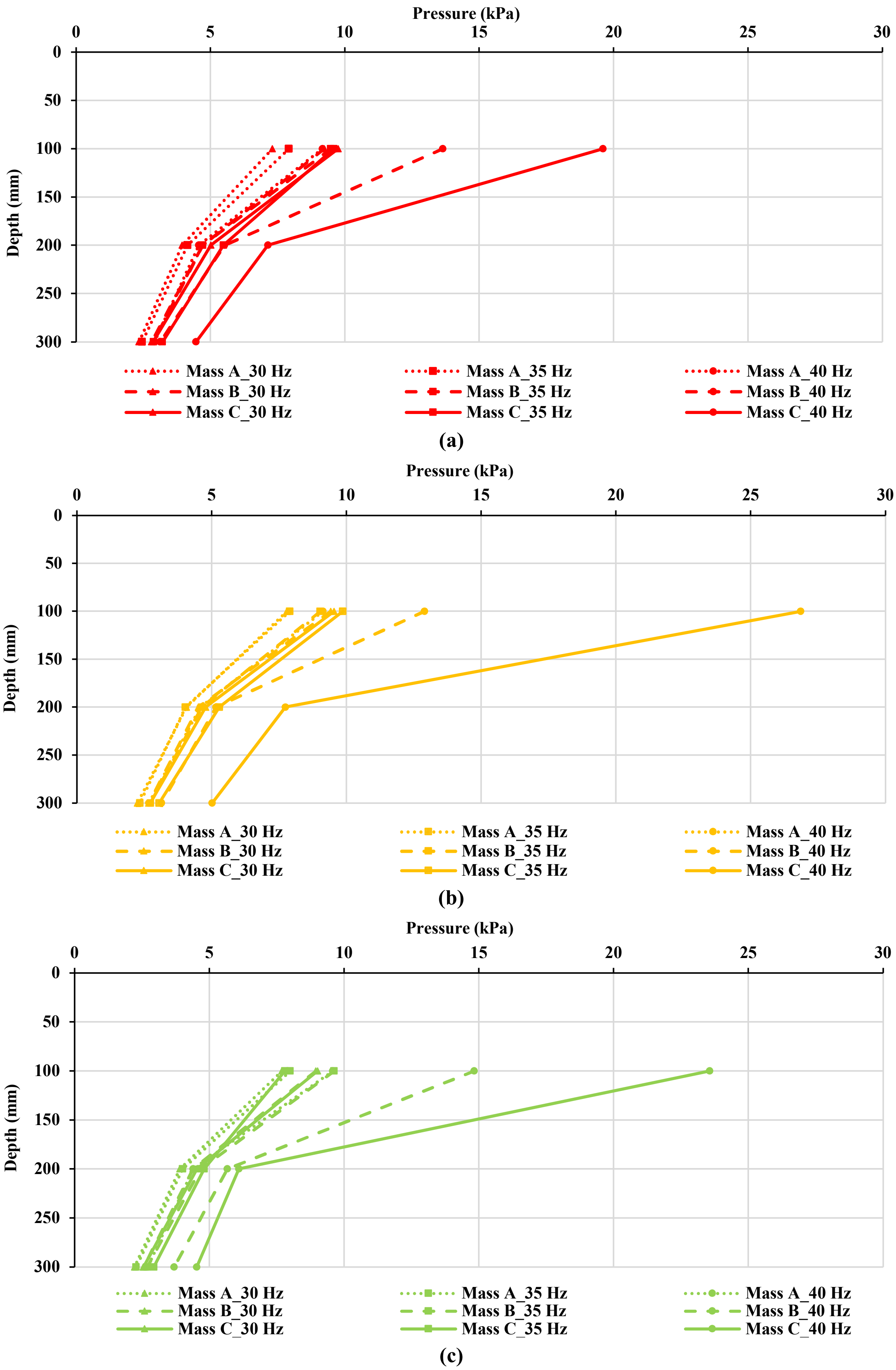

Figure 7. Peak vertical pressure–depth responses for varying vibration frequencies and eccentric mass conditions of the LVDR-2 at translational speeds of: (a) 1 km/h; (b) 4 km/h; and (c) 7 km/h.

Figure 8 presents the measured peak vertical pressures plotted against depth for varying translational speeds of the LVDR-2 model under eccentric mass configurations of Mass A, Mass B, and Mass C. Subfigures 8a, 8b, and 8c show the results obtained at constant vibration frequencies of 30 Hz, 35 Hz, and 40 Hz, respectively enabling direct comparison of the effects of translational speed and eccentric mass on subsurface pressure transmission.

At vibration frequencies of 30 Hz and 35 Hz, the highest peak pressures at a depth of 100 mm were observed under the eccentric Mass C configuration, occurring at operating speeds of 1 km/h and 4 km/h, respectively. In both cases, the maximum peak pressure was approximately 10 kPa. In contrast, at a vibration frequency of 40 Hz, a substantially higher maximum peak pressure of approximately 27 kPa was recorded at an operating speed of 4 km/h, also under the Mass C configuration. It is evident from Figure 8 that the Mass C configuration consistently produced the highest peak pressures across all vibration frequencies investigated in this study.

From Figure 8, it can be observed that higher vibration frequencies enhanced the transmission of dynamic energy, consistent with observations reported in previous vibratory compaction studies [17, 18, 20]. Conversely, lower vibration frequencies resulted in comparatively reduced peak pressure responses irrespective of translational speed and eccentric mass configuration, thereby limiting stress propagation at depth during vibratory compaction.

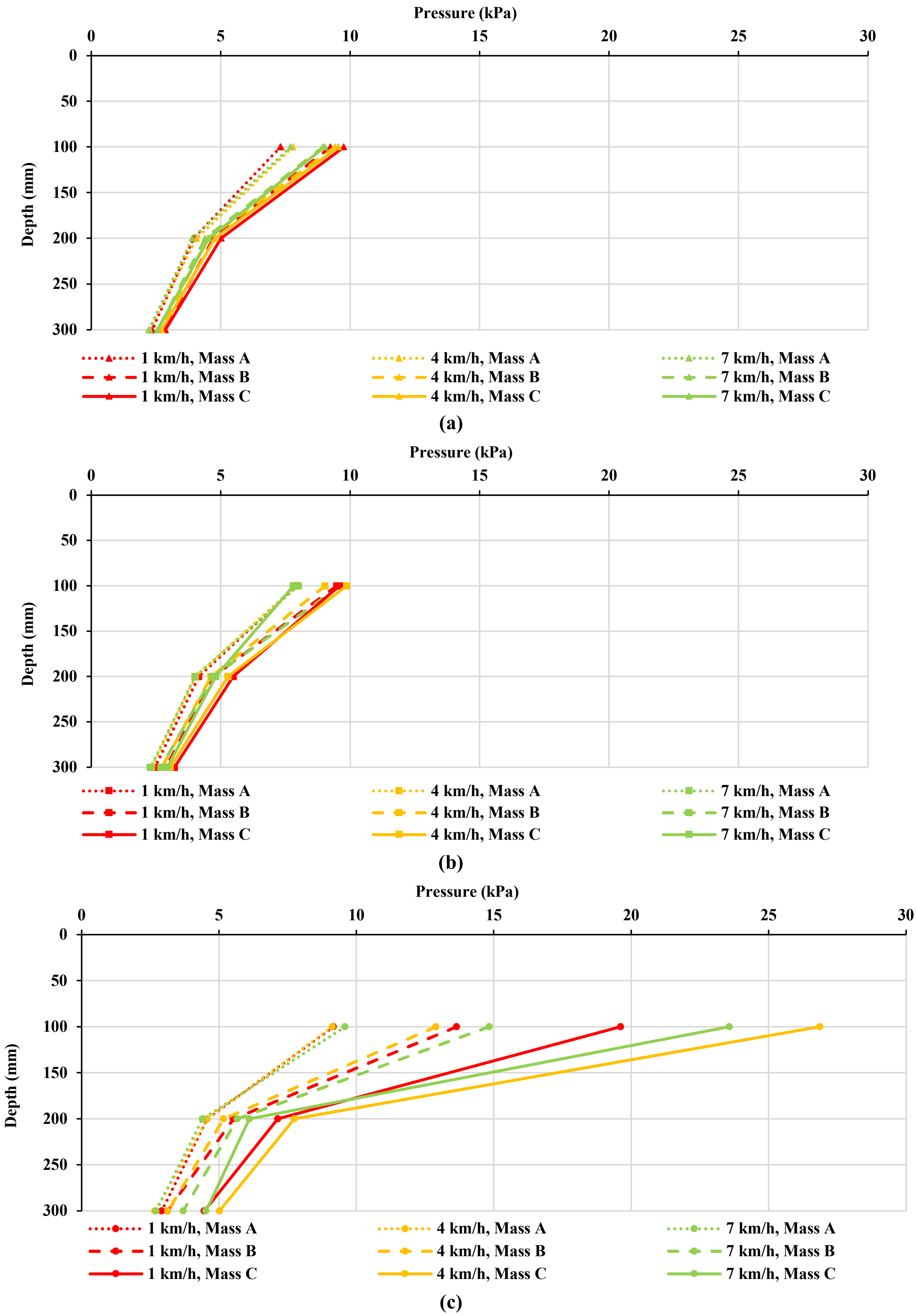

Figure 8. Peak vertical pressure–depth responses for varying translational speeds of the LVDR-2 under three eccentric mass configurations at fixed vibration frequencies of: (a) 30 Hz; (b) 35 Hz; and (c) 40 Hz.

Figure 9 presents the measured peak vertical pressure–depth responses for varying translational speeds under vibration frequencies of 30 Hz, 35 Hz, and 40 Hz. Figures 9a, 9b, and 9c correspond to eccentric masses of Mass A, Mass B, and Mass C, respectively. Within each eccentric mass configuration, translational speed was varied across 1 km/h, 4 km/h, and 7 km/h, while vibration frequency was varied across 30 Hz, 35 Hz, and 40 Hz, enabling direct evaluation of their combined influence on subsurface pressure transmission within LHS-1E.

For the eccentric mass configurations of Mass A and Mass B, the highest peak pressures at a depth of 100 mm were observed at an operating speed of 7 km/h at 40 Hz vibration frequency, with peak pressure responses of approximately 10 kPa and 15 kPa, respectively. However, under the highest eccentric mass configuration of Mass C, the maximum peak pressure of approximately 27 kPa was recorded at an operating speed of 4 km/h at 40 Hz vibration frequency.

The heaviest eccentric mass configuration, Mass C, consistently produced greater pressures than the lower eccentric mass configurations across the range of translational speeds and vibration frequencies tested. The increased eccentric mass generated greater centrifugal forces within the drum assembly, enabling more effective transfer of vibratory energy into the simulant and resulting in enhanced stress propagation with depth, consistent with established vibratory roller behaviour [20, 27].

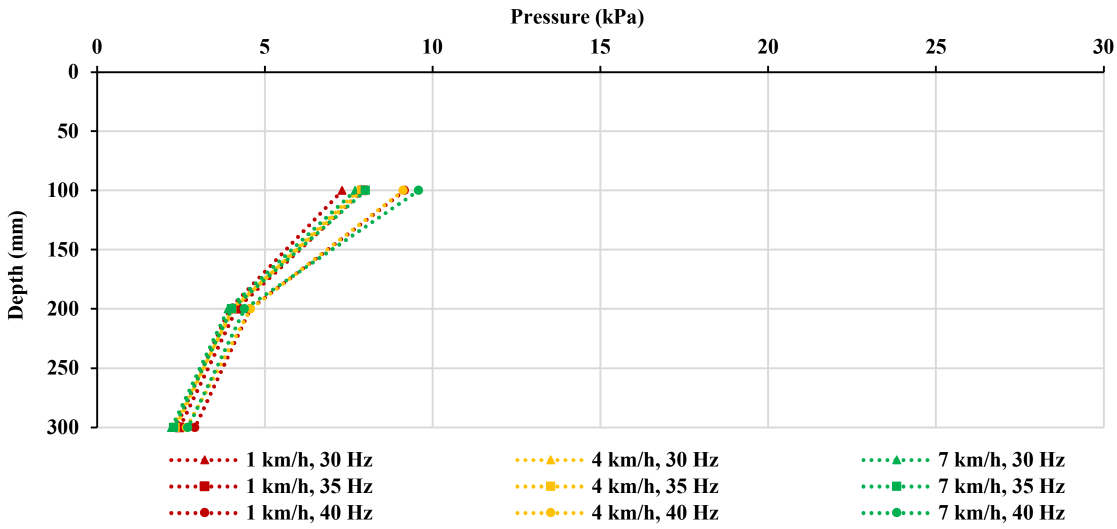

(a)

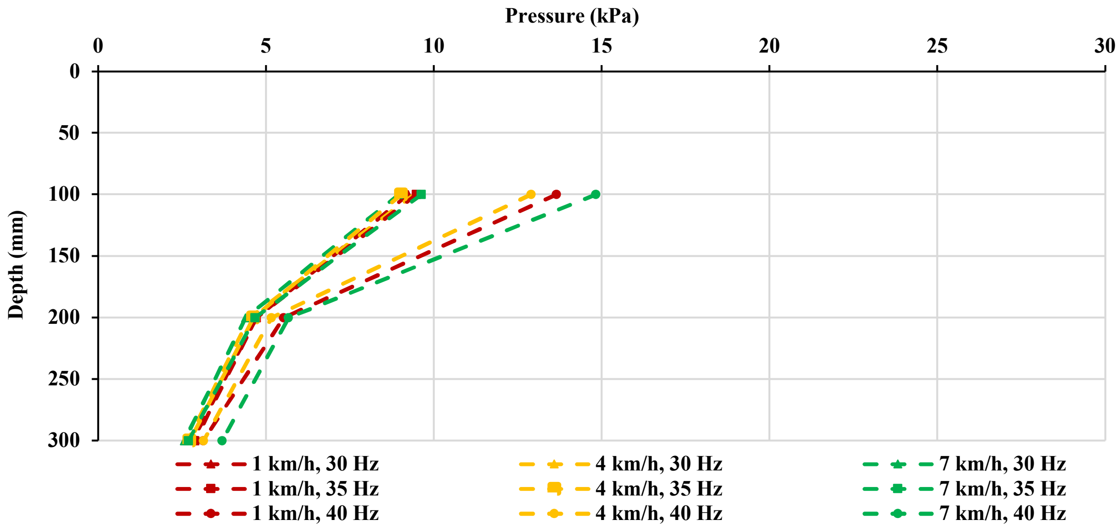

(b)

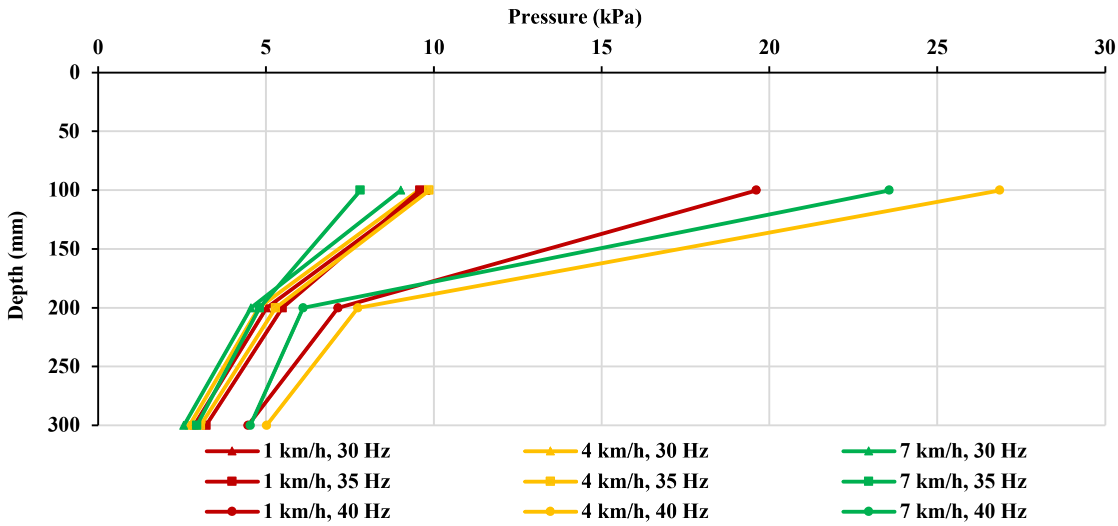

(c)

Figure 9. Peak vertical pressure–depth responses for varying vibration frequencies and translational speeds of the LVDR-2 under eccentric mass conditions of: (a) Mass A (21.8 g); (b) Mass B (49.8 g); and (c) Mass C (75.8 g).

Figure 10 presents the vertical acceleration response measured over a one-second interval, spanning 0.5 seconds on either side of the time corresponding to the peak pressure response at an EPC depth of 100 mm for selected operating combinations. Figures 10a, 10b, 10c and 10d correspond to the 340th pass at 4 km/h, 40 Hz and Mass C; the 350th pass at 7 km/h, 40 Hz and Mass C; the 310th pass at 4 km/h, 35 Hz and Mass C; and the 260th pass at 7 km/h, 40 Hz and Mass B, respectively.

Figure 10 demonstrates that the vertical acceleration response was strongly influenced by both vibration frequency and eccentric mass. A comparison of Figures 10a and 10c, where the translational speed (4 km/h) and eccentric mass (Mass C) were held constant while the vibration frequency increased from 35 Hz to 40 Hz, shows a substantial increase in the peak vertical acceleration from approximately 0.4 g to 1.3 g. This indicates that increasing the vibration frequency markedly enhanced the dynamic response of the LVDR-2 model.

Similarly, comparison of Figures 10b and 10d, where the translational speed (7 km/h) and vibration frequency (40 Hz) were maintained constant while the eccentric mass increased from Mass B to Mass C, reveals a pronounced increase in the peak vertical acceleration from approximately 0.2 g to 1.1 g. These results demonstrate that increasing the eccentric mass also substantially amplified the vertical acceleration response. Overall, the findings indicate that both higher vibration frequency and larger eccentric mass significantly enhanced the dynamic excitation generated by the LVDR-2 model, which is consistent with the greater pressure transmission and compaction performance observed in the preceding results.

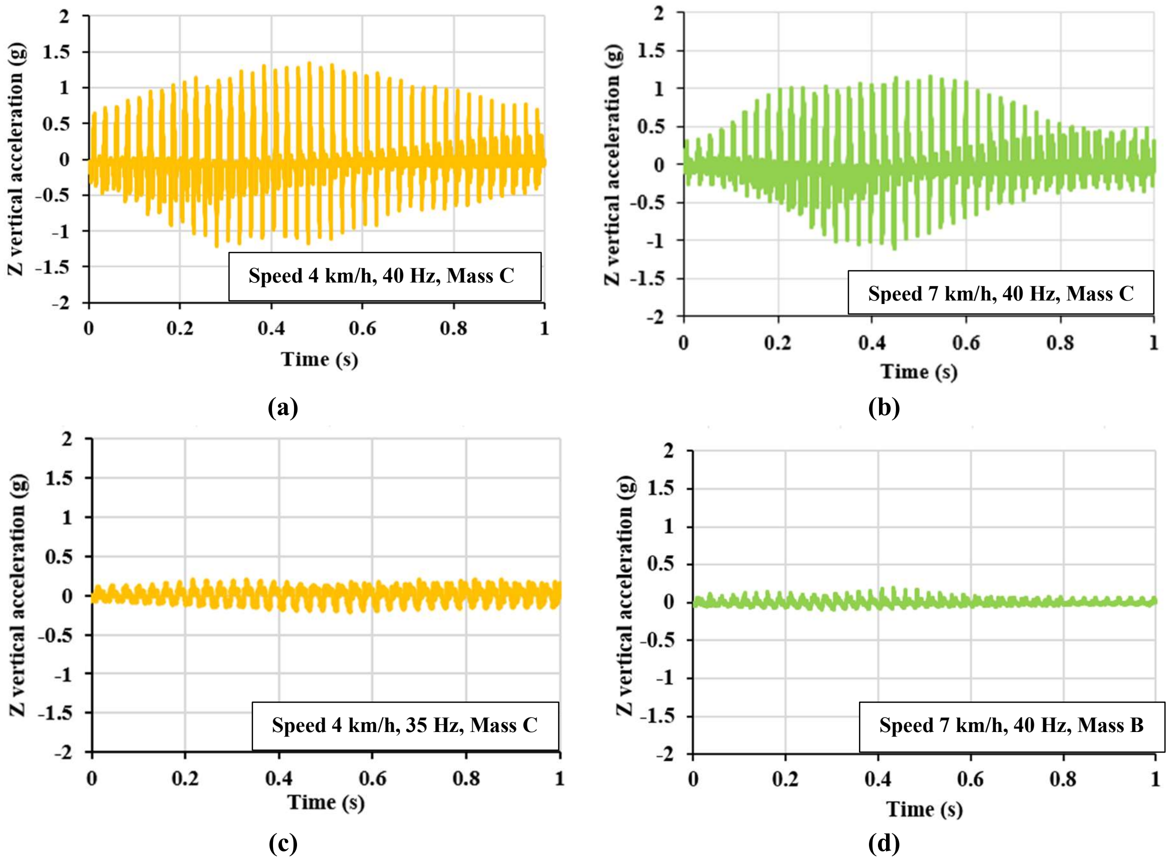

Figure 10. Vertical acceleration vs time responses measured at a depth of 100 mm beneath the roller drum over a 1-second interval: (a) 4 km/h, 40 Hz, Mass C; (b) 7 km/h, 40 Hz, Mass C; (c) 4km/h, 35 Hz, Mass C; (d) 7 km/h, 40 Hz, Mass B.

To further examine the dynamic behaviour of the simulant within the influence zone beneath the roller drum, a 0.1-second segment of the acceleration responses, previously presented in Figures 10a and 10b, is enlarged and shown in Figures 11a and 11b, respectively. Figures 11a and 11b illustrate the vertical acceleration–time response of the simulant during cyclic vibratory loading. An initial downward (negative) acceleration occurs as the roller drum applies dynamic loading to the simulant surface. Following this loading phase, resistance within the compacted simulant is mobilised, resulting in an upward acceleration response. The acceleration amplitude subsequently decreases and gradually approaches equilibrium prior to the commencement of the next vibration cycle.

The interval between successive acceleration cycles is approximately 0.025 s, corresponding to the operating vibration frequency of 40 Hz applied during testing. The observed cyclic acceleration behaviour demonstrates the repeated loading–unloading response induced by the vibratory drum mechanism during compaction. The comparatively higher acceleration amplitudes observed under lower translational speed conditions further indicate increased transmission of vibratory energy into the simulant. The increased acceleration response observed at lower speed is likely associated with the longer duration of roller–simulant interaction during each vibration cycle, allowing greater transmission of vibratory energy into the simulant. This behaviour is consistent with observations reported in previous investigations by Agarwal et al. [17, 18].

Future investigations should therefore focus on detailed assessment of acceleration amplitude variations under different operating conditions to establish clearer relationships between vibratory energy transmission, stiffness evolution, and compaction performance within lunar regolith simulants.

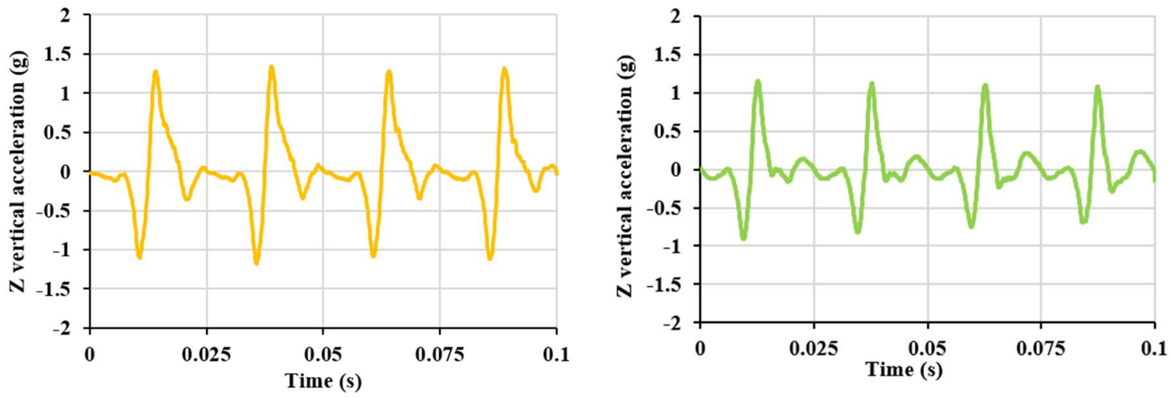

(a) (b)

Figure 11. Zoomed vertical acceleration–time responses measured beneath the roller drum over a 0.1-second interval at a depth of 100 mm under a constant eccentric mass of 75.8 g and vibration frequency of 40 Hz for translational speeds of: (a) 4 km/h; and (b) 7 km/h.

Figures 7, 8 and 9 demonstrate that peak vertical pressures were greatest near the surface and progressively decreased with increasing depth, consistent with previous vibratory compaction investigations reported by Agarwal et al. [6, 7, 17, 18] and Rinehart and Mooney [23]. However, the rate of attenuation varied significantly depending on the operating parameters applied. Although peak pressures decreased with depth, the 4 km/h, 40 Hz, and Mass C (75.8 g) eccentric mass configuration consistently produced the highest pressure responses at the measured depths of 100 mm, 200 mm, and 300 mm compared with the remaining speed–frequency- eccentric mass combinations tested in the LVDR-2 model. This observation is consistent with the surface settlement and acceleration-time response results, which also demonstrated greater densification under the same operating combinations.

4. STAGE 2 METHODOLOGY

Following completion of Stage 1, the optimal operating combination was adopted for subsequent testing. This stage of testing focused on evaluating changes in the geotechnical behaviour of the simulant resulting from vibratory compaction, including surface settlement, peak vertical pressure response, bulk density, cone penetration resistance, and vane shear strength.

The simulant was placed in a loose condition to replicate the relatively unconsolidated nature of the lunar surface and to evaluate the capability of the LVDR-2 model to improve the densification and geotechnical characteristics of the simulant through vibratory compaction. A target bulk density of 1550 kg/m³ was adopted for the LHS-1E simulant. This density represents a loose regolith simulant condition that can be reproducibly achieved under terrestrial laboratory conditions and is typical of the density of near-surface lunar regolith. The adopted placement density falls within the typical lunar regolith density range of approximately 870 kg/m³ to 1930 kg/m³ reported from Apollo mission samples and documented in the Lunar Sourcebook [3]. However, due to the inability to replicate key lunar environmental conditions, including vacuum exposure, reduced gravitational acceleration, and the presence of agglutinates, the lower-bound densities reported for in situ lunar regolith could not be reproduced under terrestrial laboratory conditions [3]. To define the achievable density range for the simulant, minimum and maximum dry densities of 1450 kg/m³ and 2000 kg/m³, respectively, were determined in accordance with AS 1289.5.5.1 [32], as previously reported by Agarwal et al. [10]. Based on these minimum and maximum density values and using Eq. (1), the adopted initial placement density corresponds to a relative density of approximately 23%.

$$RD(\%) = \frac{\rho_{max}}{\rho} \times \frac{\rho - \rho_{min}}{\rho_{max} - \rho_{min}} \times 100 \quad (1)$$

where ρ, ρ_{min}, and ρ_{max} represent the in situ, minimum, and maximum dry densities of the simulant, respectively. Based on the adopted placement density and bin geometry, approximately 468 kg of LHS-1E simulant was placed within each test bin prior to compaction testing.

To achieve a homogeneous placement density throughout each bin, the simulant was weighed and carefully placed using 5-litre buckets. The LHS-1E simulant was pluviated through a 2.36 mm sieve, while the fall height was controlled to remain below 200 mm to achieve a loose placement condition and maintain uniformity of the initial density throughout both test bins. To further enhance placement consistency, the simulant was placed in 50 mm thick layers and screeded against timber formwork installed around the perimeter of the bins, thereby enabling consistent layer thickness and surface levelling throughout placement. Although the placement procedure was time-intensive, subsequent density measurements demonstrated good agreement with the target placement density. Placement of the simulant was further complicated by significant dust generation due to the desiccated nature and high fines content of the LHS-1E material. Accordingly, appropriate personal protective equipment, including safety glasses, respiratory masks, coveralls, and gloves, was worn throughout handling and placement of the simulant to address associated health and safety considerations during testing.

Figure 12 illustrates a schematic of the configuration adopted for the detailed geotechnical testing, including the lane arrangement, rolling direction, and testing locations. The central test lane was compacted using the optimal operating combination identified during Stage 1. Figure 12a additionally identifies the locations of the geotechnical tests conducted to evaluate the influence of the LVDR-2 model on the densification behaviour and uniformity of the LHS-1E simulant.

Figure 12b illustrates the arrangement of the EPCs embedded within the simulant. Three EPCs were installed in Bin A at depths of 100 mm, 200 mm, and 300 mm below the simulant surface. The EPCs were positioned at vertical intervals of 100 mm and laterally offset by 100 mm to minimise potential sensor interaction effects during vibratory loading. For each depth, representative peak pressure values were determined by averaging measurements obtained from 20 roller passes.

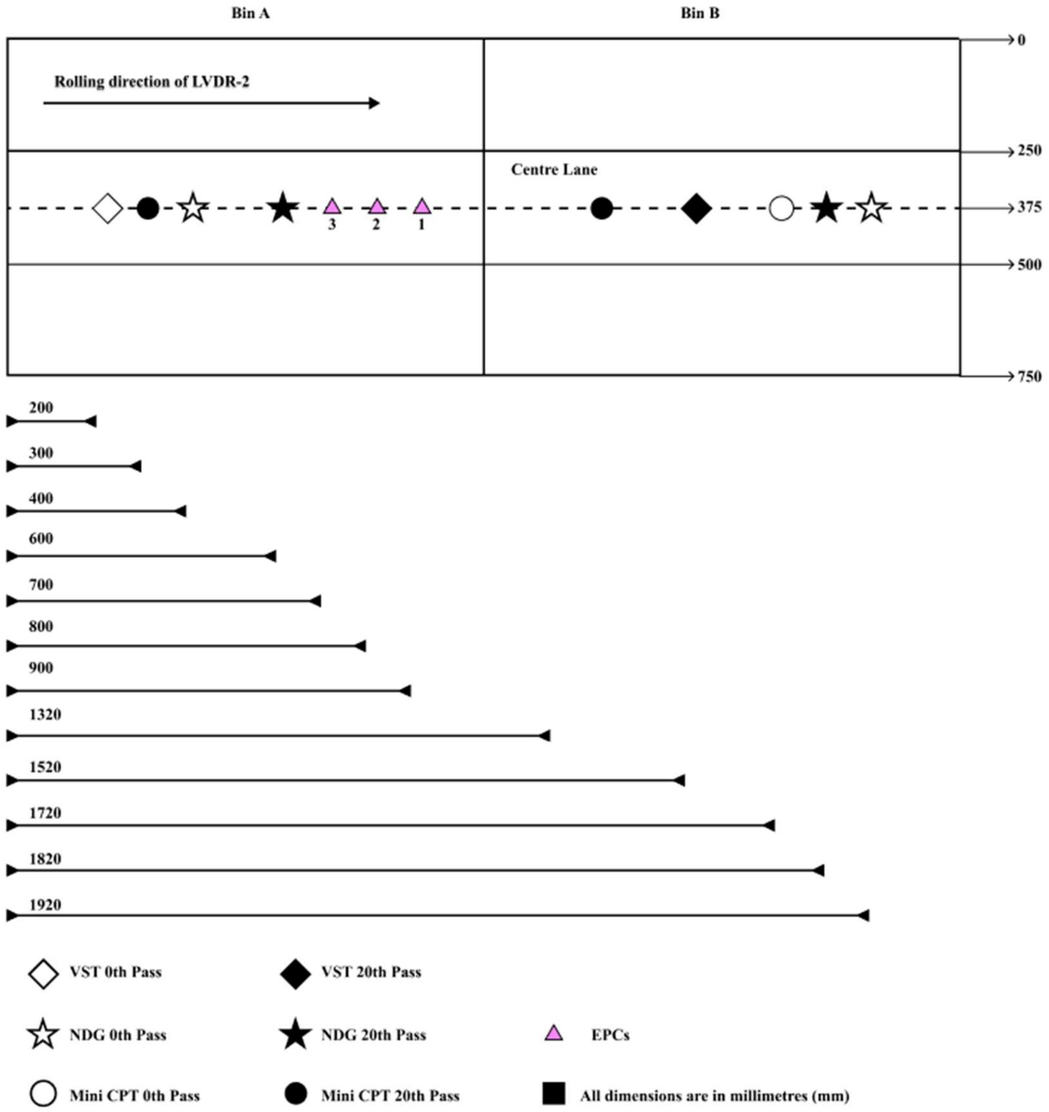

(a)

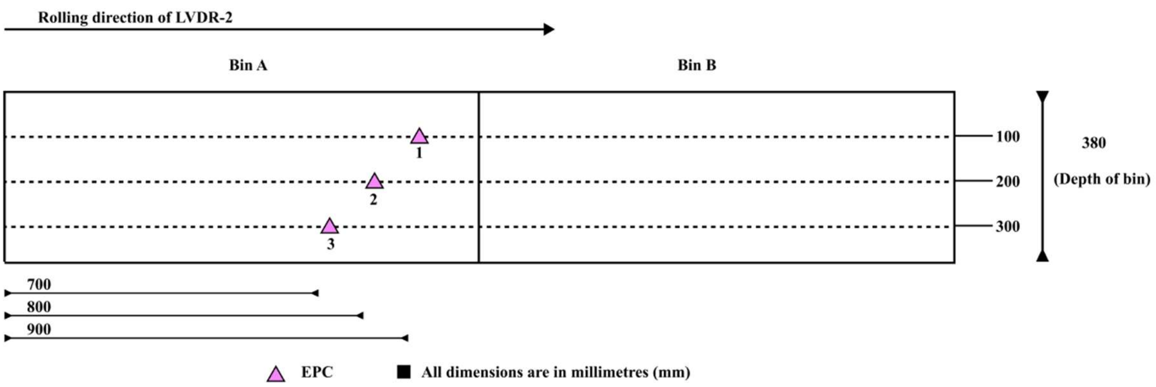

(b)

Figure 12. Schematic configuration of the detailed geotechnical testing showing: (a) plan view of the testing locations and rolling direction; and (b) elevation view of the EPC arrangement and embedment depths.

Surface settlement measurements were conducted using the same measurement procedure described previously for Stage 1.

In situ density measurements were obtained using a nuclear density gauge (NDG) HS-5001SD [33] in accordance with the manufacturer's operating manual [34] and the relevant Australian Standard [35]. The NDG determines in situ density through gamma radiation attenuation using a caesium-137 source and is widely adopted for field density assessment of compacted soils due to its rapid and relatively non-destructive measurement capability [36]. Density measurements were conducted prior to compaction and following completion of 20 passes of the LVDR-2 model within the centre test lane. Owing to the limited dimensions of the testing bins, measurements were obtained at two predetermined locations along the centre lane at the 0-pass condition and after completion of the 20th pass, as illustrated in Figure 12a. Density readings were initially obtained at a depth of 50 mm, followed by measurements at 25 mm depth intervals to a maximum depth of 300 mm. At each depth, three measurements were recorded and averaged to determine the representative in situ density. Where the variation between measurements exceeded 0.5%, an additional measurement was conducted at the corresponding depth to ensure consistency and repeatability of the recorded density values.

Mini cone penetration tests (mini-CPTs) were conducted using a Geomil digital cone penetrometer equipped with a 25 mm shaft diameter, a cone cross-sectional area of 500 mm^2, and a 60° apex angle [37]. The mini-CPT system utilises a cone mounted at the end of a penetration rod, which was manually penetrated perpendicular to the simulant surface at a penetration rate of approximately 20 mm/s in accordance with the relevant Australian Standard testing procedure [38]. Cone penetration resistance was recorded at 10 mm depth intervals, while penetration depth was monitored using a synchronised depth encoder integrated within the testing system. Mini-CPT measurements were conducted prior to compaction and after 20 roller passes within the centre test lane to evaluate changes in penetration resistance.

Vane shear testing was conducted to evaluate the shear strength behaviour of the LHS-1E before and after vibratory compaction. Testing was performed using a calibrated field vane shear tester (Model 16-T0174) in general accordance with AS 1289.6.2.1 [39]. The vane shear apparatus consisted of a four-bladed vane with dimensions of 50.8 mm in height and 25.4 mm in diameter attached to an extension rod and calibrated torque-reading mechanism [40]. The vane was manually pushed into the simulant to the required test depth while ensuring minimal disturbance during penetration. Vane shear measurements were conducted at depths of 100 mm, 200 mm, and 300 mm within the centre test lane prior to compaction and following completion of 20 roller passes to evaluate the influence of vibratory compaction on the shear resistance behaviour of the simulant. Three measurements were obtained at each testing depth for peak and remoulded shear strength, and the corresponding average values were used to represent the peak and remoulded shear strengths at each depth.

5. STAGE 2 RESULTS AND DISCUSSION

The compaction response of the simulant was assessed using measurements of in situ density, cone penetration resistance, vane shear strength, surface settlement, and subsurface pressure response to provide a comprehensive evaluation of the compaction behaviour with depth.

Figure 13 presents the variation in surface settlement with increasing roller passes for the LVDR-2 scale model under the optimal operating combination of 4 km/h translational speed, 40 Hz vibration frequency, and an eccentric mass of 75.8 g. A total of 20 roller passes was applied within the centre test lane of each bin.

The first roller pass produced the greatest surface settlement, consistent with previous observations reported by Agarwal et al. [6, 7, 17, 18], reflecting the very loose initial placement condition of LHS-1E. The majority of surface settlement occurred during the initial 10 roller passes. Beyond this, subsequent passes produced only marginal additional settlement, indicating progressive stabilisation of surface deformation and a reduction in the rate of densification with increasing compaction effort. This behaviour is consistent with established vibratory compaction behaviour, in which the majority of particle rearrangement and void reduction occurs during the early stages of compaction [22].

Following 10 and 20 roller passes, the measured surface settlements were approximately 23 mm and 29 mm, respectively. These results indicate that the combined influence of heavier eccentric mass, higher vibration frequency, and intermediate translational speed promoted improved densification behaviour.

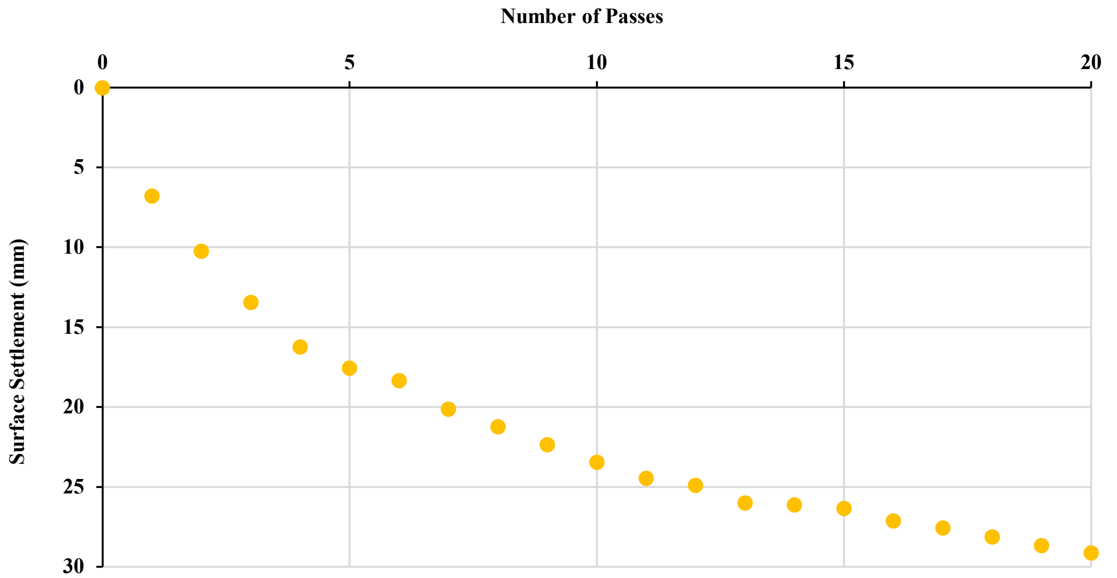

Figure 13. Surface settlement versus number of passes.

Figure 14 presents the variation in averaged peak vertical pressure with depth below the simulant surface for the LVDR-2 model operating at a translational speed of 4 km/h, vibration frequency of 40 Hz, and eccentric mass of 75.8 g. Peak pressure measurements obtained from the three EPCs installed at depths of 100 mm, 200 mm, and 300 mm were averaged over 20 roller passes at each depth to evaluate the subsurface pressure response during vibratory compaction. The highest averaged peak pressure (17 kPa) was recorded at a depth of 100 mm. In contrast, the averaged peak pressure progressively decreased with depth, reaching approximately 5 kPa at a depth of 300 mm.

The highest stress levels were therefore concentrated within the near-surface region, while progressively lower pressure magnitudes were observed at greater depths. This behaviour indicates attenuation of vibratory stress transmission with depth and is consistent with the established behaviour of vibratory compaction of granular materials [31, 41].

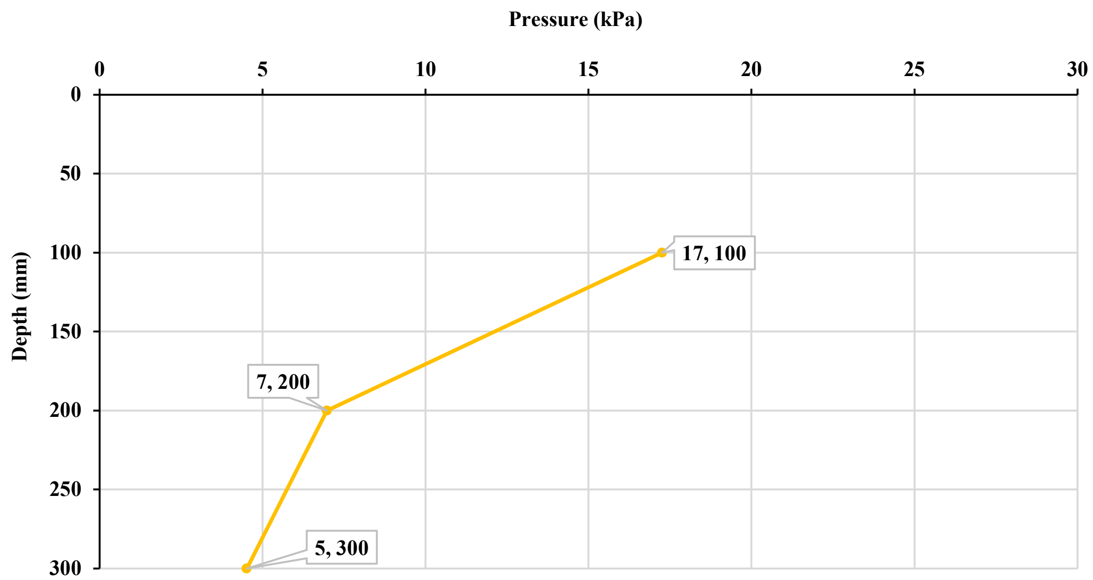

Figure 14. Variation in averaged peak vertical pressure with depth for the LVDR-2 model operating at a translational speed of 4 km/h, vibration frequency of 40 Hz, and eccentric mass of 75.8 g, averaged over 20 roller passes.

Figure 15 presents the in situ density with depth below the surface for increasing numbers of roller passes using the LVDR-2 model. Prior to compaction, the target placement density for the LHS-1E simulant was 1550 kg/m^3; however, the measured average initial in situ density following preparation of the test bins was approximately 1570 kg/m^3, corresponding to a relative density of approximately 28%. This measured density represents the average in situ density throughout the depth before vibratory compaction. The slight increase relative to the target placement density may be attributed to minor variations in particle packing and variability during placement and levelling of the simulant within the test bins. Accordingly, the measured pre-compaction density was adopted as the baseline condition for subsequent assessment of density evolution during vibratory compaction.

The results demonstrate that vibratory compaction using the LVDR-2 model produced a progressive increase in in situ density with increasing roller passes at all measured depths. At a depth of 50 mm, the measured in situ density after 20 roller passes increased to approximately 1791 kg/m^3, corresponding to a relative density of approximately 69%. This represents an increase in relative density of approximately 41% relative to the average initial placement condition. In contrast, at a depth of 300 mm, the corresponding density after 20 passes was approximately 1663 kg/m^3, corresponding to a relative density of approximately 47% and an increase in relative density of approximately 19%.

These results indicate that the vibratory energy imparted by the LVDR-2 model was most effective within the near-surface region of the simulant, where particle rearrangement and void reduction were greatest. The progressive reduction in densification with increasing depth suggests attenuation of vibratory energy transmission within the lunar highland regolith simulant during compaction. This behaviour is consistent with vibratory compaction mechanisms reported in previous studies, in which the influence of dynamic loading progressively decreases with depth beneath the roller drum [6, 7, 17, 18, 22, 31].

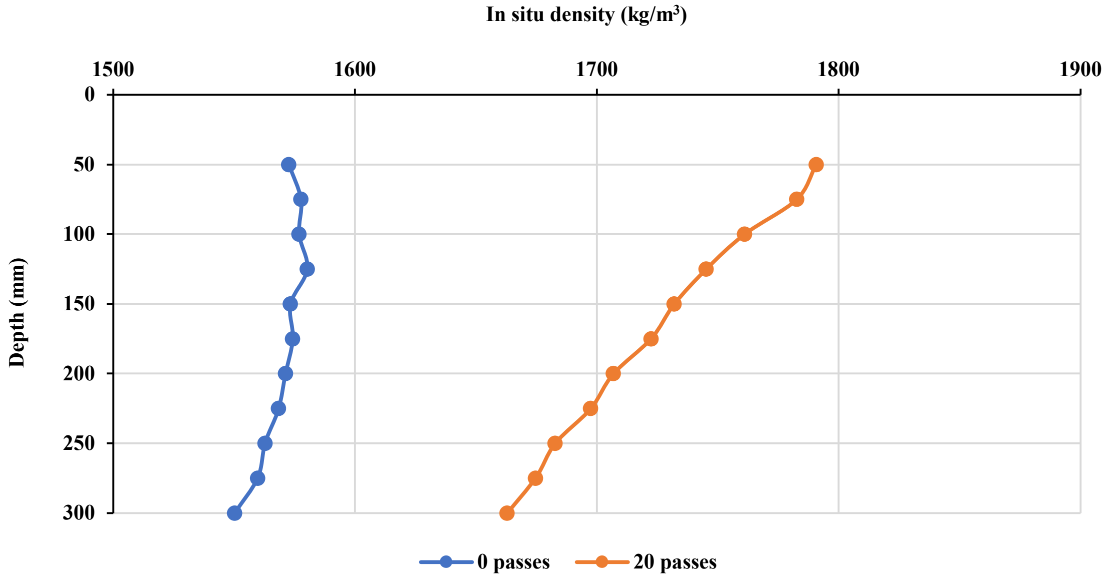

Figure 15. Measured in situ density versus depth for 0 and 20 passes.

Figure 16 illustrates the variation in cone tip resistance with depth for increasing numbers of roller passes. The pre-compaction condition (0-pass), shown in Figure 16, exhibits a gradual increase in cone tip resistance with depth, which is consistent with the expected penetration response of a soil mass with relatively uniform density, where cone resistance is primarily governed by increasing overburden stress rather than compaction-induced densification [18, 42, 43].

After 20 roller passes, the largest increase in cone tip resistance was observed at shallow depths, while the magnitude of resistance increase progressively diminished with depth. The maximum cone tip resistance of approximately 0.5 MPa was recorded at a depth of 60 mm. This behaviour indicates that the influence of vibratory compaction was greatest near the ground surface and progressively attenuated with increasing depth beneath the roller drum. The observed cone penetration response is consistent with the in situ density results.

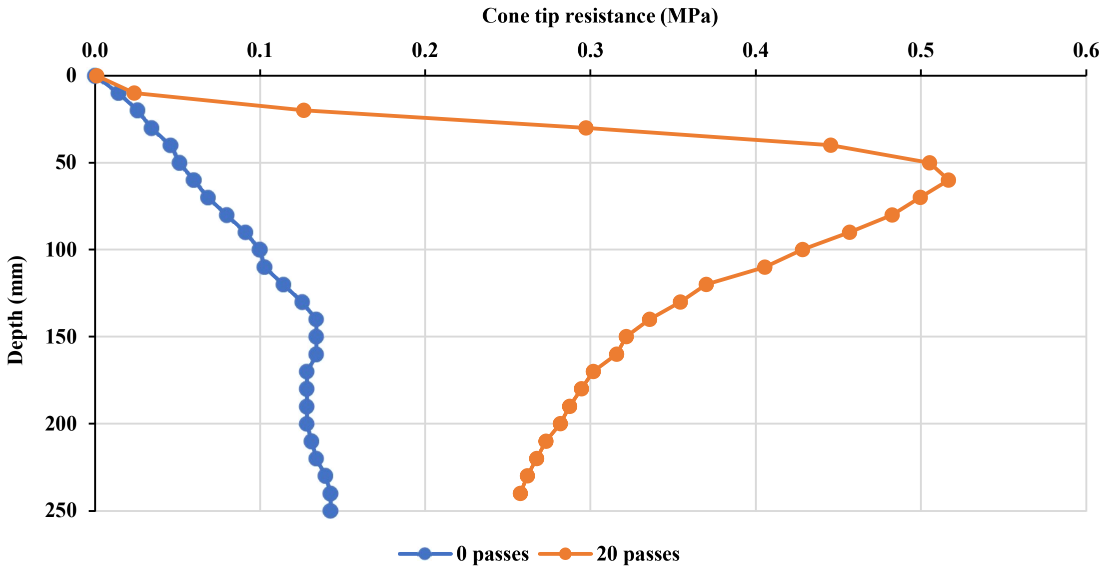

Figure 16. Resistance versus depth results are shown for 0 and 20 roller passes.

Figure 17 presents the variation in peak and residual shear strength with depth before compaction (0 passes) and following completion of 20 roller passes. Prior to compaction, the peak shear strength remained relatively uniform throughout the simulant profile, indicating that the material was prepared with broadly consistent initial shear resistance. In contrast, the residual shear strength exhibited a gradual increase with depth, reflecting the influence of increasing overburden confinement within the relatively uniform simulant. Following 20 roller passes, both peak and residual shear strengths increased considerably, although the magnitude of improvement progressively diminished with depth.

The peak shear strength profile (Figure 17a) shows that the largest increase occurred at a depth of 100 mm, where the peak shear strength increased from approximately 4 kPa under the pre-compaction condition to approximately 15 kPa after 20 passes. At a depth of 200 mm, the peak shear strength increased from approximately 3.5 kPa to 5 kPa, whereas only a negligible increase was observed at 300 mm, where the peak shear strength remained close to 4 kPa under both conditions. These results indicate that the influence of vibratory compaction was greatest nearest the surface and progressively reduced with depth.

A similar trend was observed for the residual shear strength profile (Figure 17b). Following 20 roller passes, the residual shear strength increased from approximately 2 kPa to 7 kPa at 100 mm depth and from approximately 3 kPa to 4 kPa at 200 mm depth. In contrast, the residual shear strength at 300 mm remained essentially unchanged at approximately 4 kPa, indicating that the compactive influence at this depth was limited.

The reduction in strength with depth is consistent with the attenuation of roller-induced dynamic stresses beneath the drum, as previously observed from the earth pressure cell measurements, cone penetration tests, and in situ density measurements. The negligible increase in both peak and residual shear strengths at 300 mm further indicates that, under the investigated operating combination, the effective influence of the LVDR-2 model was primarily confined to the upper 200 mm, where vibratory energy transmission and particle rearrangement were most pronounced.

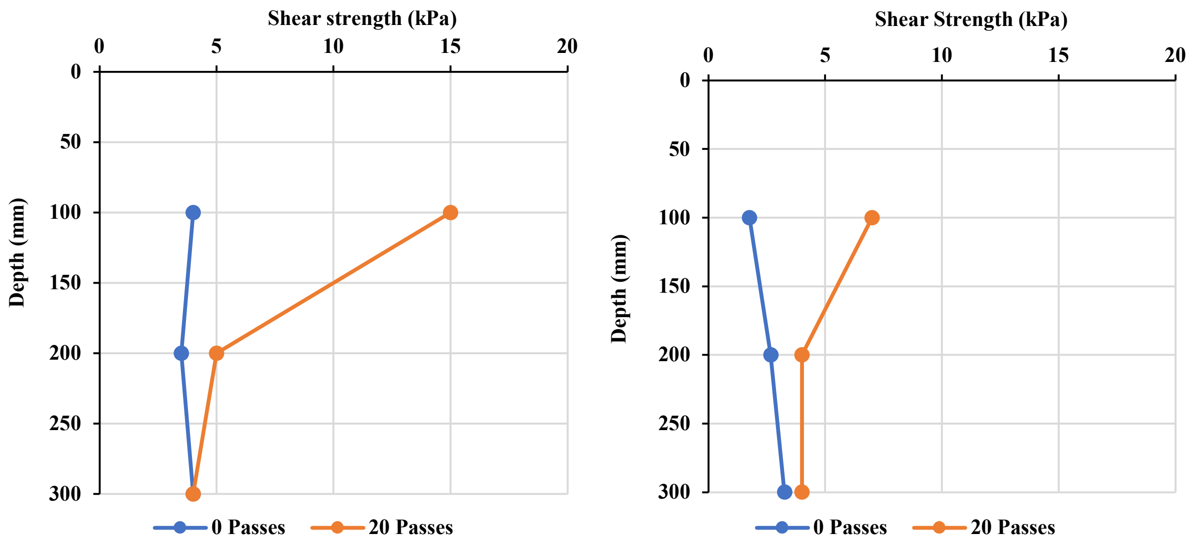

(a) (b)

Figure 16. Variations of shear strength with depth after 0 and 20 passes: (a) peak shear strength; and (b) residual shear strength.

6. CONCLUSION

This study presented the development and comprehensive experimental evaluation of a second-generation lunar vibrating drum roller (LVDR-2) scale model incorporating an internally mounted eccentric mass to more closely replicate the operating principle of full-scale vibratory smooth drum roller compaction equipment. The experimental investigation demonstrated that the redesigned vibratory mechanism substantially improved the compaction performance of engineering-grade lunar highlands regolith simulant (LHS-1E), with eccentric mass and vibration frequency exerting a greater influence on densification behaviour than translational speed.

The optimum operating combination of the LVDR-2 scale model from the 27 tested in this study, comprised a translational speed of 4 km/h, a vibration frequency of 40 Hz, and an eccentric mass of 75.8 g. This combination consistently produced the highest vertical pressures, greatest surface settlement, highest vertical acceleration, and deepest stress transmission within the simulant profile.

Compared with the previously developed LVDR-1 scale model, the optimised LVDR-2 achieved superior overall compaction performance. The LVDR-2 scale model attained a maximum bulk density of 1791 kg/m³, representing an approximately 10% increase relative to the best-performing LVDR-1 operating combination employing the 4.45 kg roller mass at 2 km/h and 40 Hz.

Across both the LVDR-1 and LVDR-2 model investigations, higher vibration frequencies consistently produced the most effective compaction response, confirming their dominant influence on stress transmission and densification of the simulant. The results further indicate that moderate translational speeds, generally within the range of 2–4 km/h, provide the most favourable compaction performance. However, translational speed had a comparatively smaller influence than vibration frequency and eccentric mass, indicating that increasing roller speed alone does not necessarily improve densification. This finding suggests that future lunar regolith compaction systems should prioritise appropriate vibration frequency and roller loading while maintaining the travelling speed within a moderate operational range.

Overall, this study advances the current understanding of vibratory compaction mechanisms in LHS-1E and provides comprehensive experimental evidence linking operating parameters, stress transmission, acceleration response, and density and strength improvement. The results of this study indicate that roller speed had a comparatively smaller influence on compaction performance than frequency and eccentric mass. The results establish an important foundation for the development of mechanised lunar ground improvement technologies capable of supporting future foundations, landing pads, mobility corridors, and ISRU infrastructure.

Although the present investigation was conducted under terrestrial laboratory conditions, the compaction behaviour of lunar regolith is expected to be influenced by reduced gravity, vacuum, and electrostatically charged particles on the lunar surface. Future work will therefore investigate the performance of the LVDR-2 under simulated lunar environmental conditions, including gravity offloading and vacuum testing, while further optimising drum geometry, eccentric mass configuration, and intelligent compaction methodologies to support future autonomous lunar construction systems.

ACKNOWLEDGEMENTS

The authors would like to acknowledge the contributions of the undergraduate students Ethan Baylas, Jared Casimiro, Hasan Mahir, Isaac Raggatt, and James Schirripa for their assistance with experimental setup, testing, and data collection. The authors also thank Kevin Farries, Rebecca Muir and William Foster-Hall from Adelaide University for their support in the design and manufacture of the lunar vibrating drum roller (LVDR-2) model and their assistance with laboratory testing. The authors further acknowledge Broons Impact Rollers for providing access to the test rig used in this study. In addition, the facilities and technical support provided by the School of Civil Engineering and Construction Management at Adelaide University are gratefully acknowledged, and Astroport Space Technologies for supporting this research.

FUNDING

This research was supported by the Andy Thomas Centre for Space Resources at Adelaide University and Astroport Space Technologies. The funding bodies had no role in the study design, data collection, analysis or interpretation, preparation of the manuscript, or the decision to submit the article for publication.

CRediT AUTHORSHIP CONTRIBUTION STATEMENT

Akshay Kumar Agarwal: Conceptualisation, Methodology, Investigation, Formal analysis, Data curation, Software, Validation, Visualisation, Writing – original draft, Writing – review and editing. Brendan Scott: Conceptualisation, Methodology, Supervision, Resources, Writing – review and editing. Mark B. Jaksa: Conceptualisation, Supervision, Writing – review and editing.

DECLARATION OF COMPETING INTEREST

The authors declare that they have no known competing financial interests or personal relationships that could have appeared to influence the work reported in this paper.

DATA AVAILABILITY

The data supporting the findings of this study are available from the corresponding author upon reasonable request.

REFERENCES

[1] National Aeronautics and Space Administration, Artemis IV, 2026. https://www.nasa.gov/mission/artemis-iv/ (accessed 30 April 2026).

[2] W.D. Carrier III, G.R. Olhoeft, W. Mendell, Physical properties of the lunar surface, in: G. Heiken, D. Vaniman, B. French (Eds.), Lunar Sourcebook: A User's Guide to the Moon, Cambridge University Press, Cambridge, UK, 1991, pp. 475–594.

[3] G.H. Heiken, D.T. Vaniman, B.M. French (Eds.), Lunar Sourcebook: A User's Guide to the Moon, Cambridge University Press, Cambridge, UK, 1991.

[4] A. Ellery, Leveraging in situ resources for lunar base construction, Can. J. Civ. Eng. 49 (5) (2022) 657–674. https://doi.org/10.1139/cjce-2021-0098.

[5] S. Zhou, C. Lu, X. Zhu, F. Li, Preparation and characterization of high strength geopolymer based on BH-1 lunar soil simulant with low alkali content, *Engineering* 7 (11) (2021) 1631–1645. https://doi.org/10.1016/j.eng.2020.10.016.

[6] A.K. Agarwal, M.B. Jaksa, B.T. Scott, Y.L. Kuo, Compaction testing on lunar highland simulant using a vibrating drum roller, in: Earth and Space 2024, American Society of Civil Engineers, 2024, pp. 763–773. https://doi.org/10.1061/9780784485736.068.

[7] A.K. Agarwal, B.T. Scott, M.B. Jaksa, Y.L. Kuo, Comparison of compaction techniques on lunar highlands regolith simulant, J. Aerosp. Eng., in press. https://doi.org/10.1061/JAEEEZ/ASENG-6822.

[8] Y.C. Toklu, P. Akpinar, Lunar soils, simulants and lunar construction materials: An overview, Adv. Space Res. 70 (3) (2022) 762–779. https://doi.org/10.1016/j.asr.2022.05.017.

[9] A. Slabic, J.E. Gruener, R.N. Kovtun, D.L. Rickman, L. Sibille, H.A. Oravec, J. Edmunson, S. Keprta, Lunar Regolith Simulant User's Guide, Rev. A, NASA/TM-20240011783, National Aeronautics and Space Administration, 2024. https://ntrs.nasa.gov/api/citations/20240011783/downloads/Lunar_Regolith_Simulant_Users_Guide_Rev_A_28OCT.pdf (accessed 30 April 2026).

[10] A.K. Agarwal, Y.L. Kuo, M.B. Jaksa, B.T. Scott, Density, strength and compressibility characteristics of lunar regolith simulant, in: Proceedings of the 14th Australia and New Zealand Conference on Geomechanics, Australian Geomechanics Society, Cairns, Queensland, Australia, 2023.

[11] Exolith Lab, LHS-1E Lunar Highlands Simulant: Fact Sheet 001-09-001-0120, n.d. https://cdn.shopify.com/s/files/1/0398/9268/0862/files/lhs-1E-spec-sheet-2021.pptx_1.pdf?v=1693316297 (accessed 30 April 2026).
[12] L.E. Bernold, Compaction of lunar-type soil, J. Aerosp. Eng. 7 (2) (1994) 175–187. https://doi.org/10.1061/(ASCE)0893-1321(1994)7:2(175).
[13] B.M. Das, K. Sobhan, Principles of Geotechnical Engineering, 8th ed., Cengage Learning, Stamford, CT, 2014.
[14] K. Terzaghi, R.B. Peck, G. Mesri, Soil Mechanics in Engineering Practice, 3rd ed., John Wiley & Sons, 1996.
[15] M.W. Hilburger, Excavation, Construction, and Outfitting (ECO): Envisioned Future Priorities, NASA, 2023. https://www.nasa.gov/wp-content/uploads/2023/06/live-eco-envisioned-future-priorities-2023-v2-final-tagged.pdf (accessed 30 April 2026).
[16] B.T. Scott, Y.L. Kuo, M.B. Jaksa, A.K. Agarwal, Compaction trial on lunar regolith simulant, in: Proceedings of the 14th Australia and New Zealand Conference on Geomechanics, Australian Geomechanics Society, Cairns, Queensland, Australia, 2023.
[17] A.K. Agarwal, B.T. Scott, M.B. Jaksa, Optimising speed and frequency of a scale model vibrating smooth drum roller on lunar highland regolith simulant, engrXiv preprint, 2026. https://doi.org/10.31224/6434.
[18] A.K. Agarwal, B.T. Scott, M.B. Jaksa, Compaction performance of a scale model vibrating drum roller on lunar highlands regolith simulant, engrXiv preprint, 2026. https://doi.org/10.31224/6983.
[19] O.Y. Chung, B.T. Scott, M.B. Jaksa, Y.L. Kuo, D. Airey, Physical modelling of rolling dynamic compaction, in: Proceedings of the 19th International Conference on Soil Mechanics and Geotechnical Engineering, International Society for Soil Mechanics and Geotechnical Engineering, Seoul, Korea, 2017, pp. 905–908.
[20] D. Adam, F. Kopf, Operational devices for compaction optimization and quality control (continuous compaction control and light falling weight device), in: A. Gomes Correia, A. Loizos (Eds.), Proceedings of the International Seminar on Geotechnics in Pavement and Railway Design and Construction, Athens, Greece, 2004, pp. 97–106.
[21] C. Wersäll, I. Nordfelt, S. Larsson, Soil compaction by vibratory roller with variable frequency, Géotechnique 67 (3) (2017) 272–278. https://doi.org/10.1680/jgeot.16.P.051.
[22] M.A. Mooney, R.V. Rinehart, Field monitoring of roller vibration during compaction of subgrade soil, J. Geotech. Geoenviron. Eng. 133 (3) (2007) 257–265. https://doi.org/10.1061/(ASCE)1090-0241(2007)133:3(257).
[23] R.V. Rinehart, M.A. Mooney, Measurement of roller compactor induced triaxial soil stresses and strains, Geotech. Test. J. 32 (4) (2009) 347–357. https://doi.org/10.1520/GTJ101889.
[24] B.T. Scott, M.B. Jaksa, P. Mitchell, Ground response to rolling dynamic compaction, Geotech. Lett. 9 (2) (2019) 99–105. https://doi.org/10.1680/jgele.18.00208.
[25] T.N. Dave, S.M. Dasaka, A review on pressure measurement using earth pressure cell, Int. J. Earth Sci. Eng. 4 (6 SPL) (2011) 1031–1034.

https://www.civil.iitb.ac.in/~dasaka/papers/trudeep_dasaka_IJESE_2012.pdf (accessed 30 April 2026).

[26] H. Henrich, Compaction with vibratory rollers, Civ. Eng. S. Afr. 29 (12) (1987) 479–481. https://journals.co.za/doi/abs/10.10520/AJA10212019_16797 (accessed 30 April 2026).

[27] Caterpillar Inc., *Caterpillar Performance Handbook*, 50th ed., Publication No. SEBD0351-50, Caterpillar Inc., Peoria, IL, USA, 2022. https://www.ringpower.com/media/oujnpuga/caterpillarperfhandbook_ed50.pdf (accessed 30 April 2026).

[28] P.J. van Susante, M.A. Mooney, Capturing nonlinear vibratory roller compactor behavior through lumped parameter modeling, J. Eng. Mech. 134 (8) (2008) 684–693. https://doi.org/10.1061/(ASCE)0733-9399(2008)134:8(684).

[29] A. Altaee, B.H. Fellenius, Physical modeling in sand, Can. Geotech. J. 31 (3) (1994) 420–431. https://doi.org/10.1139/t94-049.

[30] R.D. Holtz, W.D. Kovacs, T.C. Sheahan, An Introduction to Geotechnical Engineering, 2nd ed., Pearson, Upper Saddle River, NJ, 2011.

[31] F.E. Richart Jr., J.R. Hall Jr., R.D. Woods, Vibrations of Soils and Foundations, Prentice-Hall, 1970.

[32] Standards Australia, Methods of Testing Soils for Engineering Purposes—Method 5.5.1: Soil Compaction and Density Tests—Determination of the Minimum and Maximum Dry Density of a Cohesionless Material—Standard Method, AS 1289.5.5.1-1998, Standards Australia, Sydney, Australia, 1998.

[33] Humboldt Mfg. Co., HS-5001SD Nuclear Density Gauge, n.d. https://www.humboldtmfg.com/nuclear-gauge-hs-5001sd.html (accessed 30 April 2026).

[34] Humboldt Scientific, Inc., HS-5001SD Moisture-Density Gauge: Product Manual, Humboldt Scientific, Inc., 2020. https://www.humboldtmfg.com/manuals/HS-5001SD_MANUAL%20_0920.pdf (accessed 30 April 2026).

[35] Standards Australia, Methods of Testing Soils for Engineering Purposes—Method 5.8.1: Soil Compaction and Density Tests—Determination of Field Density and Field Moisture Content of a Soil Using a Nuclear Surface Moisture–Density Gauge—Direct Transmission Mode, AS 1289.5.8.1-2007, Standards Australia, Sydney, Australia, 2007.

[36] A. Bretreger, Technical Guide L-G-002: Field density testing using a nuclear density gauge, Roads and Maritime Services, NSW Government, Australia, 2015.

[37] Geomil Equipment B.V., D-cone: Digital CPT Cone and Geotechnical Sensor Network (GSN), n.d. https://www.geomil.com/products/d-cone (accessed 30 April 2026).

[38] Standards Australia, Methods of Testing Soils for Engineering Purposes—Method 6.5.1: Soil Strength and Consolidation Tests—Determination of the Static Cone Penetration Resistance of a Soil—Field Test Using a Mechanical and Electrical Cone or Friction-Cone Penetrometer, AS 1289.6.5.1-1999, Standards Australia, Sydney, Australia, 1999.

[39] Standards Australia, Methods of Testing Soils for Engineering Purposes—Method 6.2.1: Soil Strength and Consolidation Tests—Determination of the Shear Strength of a

Soil—Field Test Using a Vane, AS 1289.6.2.1-2001, Standards Australia, Sydney, Australia, 2001.

[40] C-Tech Laboratory Equipment Co., Ltd., Field Vane Shear Tester 16-T0174: Product Manual, C-Tech Laboratory Equipment Co., Ltd., n.d.

[41] K.R. Massarsch, B.H. Fellenius, Deep vibratory compaction of granular soils, in: B. Indraratna, J. Chu (Eds.), Ground Improvement: Case Histories, Elsevier Geo-Engineering Book Series, vol. 3, Elsevier, 2005, pp. 539–561. https://doi.org/10.1016/S1571-9960(05)80022-9.

[42] T. Lunne, J.J.M. Powell, P.K. Robertson, Cone Penetration Testing in Geotechnical Practice, CRC Press, Boca Raton, FL, 2002. https://doi.org/10.1201/9781482295047.

[43] P.K. Robertson, Interpretation of cone penetration tests—a unified approach, Can. Geotech. J. 46 (11) (2009) 1337–1355. https://doi.org/10.1139/T09-065.